

Development of a Plume Model and Application to  
Mars 2001 Odyssey Aerobraking

By

Zachary Quinn Chavis

B.S. in Mechanical Engineering, May 2000, University of Texas

A Thesis submitted to

The faculty of

The School of Engineering and Applied Science

of The George Washington University

in partial satisfaction of the requirements for the degree of

Master of Science

August 31, 2002

Thesis directed by

Robert H. Tolson

Professor of Engineering and Applied Science

This research was conducted at NASA Langley Research Center

## **Abstract**

A modified source flow model was used to calculate the plume flowfield from a Mars Odyssey thruster during aerobraking. The source flow model results compared well with previous detailed CFD results for a Mars Global Surveyor thruster. Using an iso-density surface for the Odyssey plume, DSMC simulations were performed to determine the effect the plumes have on the Odyssey aerodynamics. A database was then constructed to incorporate the plume effects into 6-DOF simulations over a range of attitudes and densities expected during aerobraking. 6-DOF simulations that included the plume effects showed better correlation with flight data than simulations without the plume effects.

## **Acknowledgments**

The author would like to thank Dr. Richard G. Wilmoth for his guidance and advice during the research and for his time spent editing papers. The author would also like to thank Dr. Christopher E. Glass for his assistance and use of his CFD results, Jill Hanna for her assistance with the POST simulations, and Dr. Robert H. Tolson for his advice.

The author would like to express appreciation to the faculty, staff, and fellow students of the George Washington University's Joint Institute for Advancement of Flight Sciences for making the past two years very enjoyable and rewarding.

## Table of Contents

Abstract.....	iii
Acknowledgments.....	iv
Table of Contents.....	v
List of Figures.....	vii
List of Tables.....	viii
Nomenclature.....	ix
Chapter 1. Introduction.....	1
Chapter 2. Mars Odyssey Mission.....	4
0.1 Objectives.....	4
0.2 Aerobraking.....	5
Chapter 3. Development of a Source Flow Plume Model.....	8
0.1 Internal Nozzle Flow Calculations.....	9
0.2 Theory of Source Flow Model.....	13
0.3 Modifications Made to Source Flow Model.....	17
Chapter 4. Plume Model Validation.....	23
0.1 MGS Comparison.....	23
0.2 Boundary Layer Sensitivity.....	29
Chapter 5. Plume-Flowfield Interaction Modeling.....	32
0.1 Rarefied Flow.....	32
0.2 Direct Simulation Monte Carlo.....	33
Chapter 6. Parametric Study.....	37
0.1 Grid Resolution.....	37
0.2 Source Flow Model.....	40
Chapter 7. Application to Mars 2001 Odyssey.....	44
0.1 Baseline Aerodynamics.....	44
0.2 RCS Study.....	46
0.3 RCS Database Construction.....	50

0.4	Effects on the Aerodynamics.....	57
Chapter 8.	Validation of Application to Mars Odyssey.....	59
0.1	POST Simulation Results.....	59
0.2	Flight Data Comparison.....	60
Chapter 9.	Conclusions.....	68
Chapter 10.	Future Work.....	71
References.....		72

## List of Figures

2.1 Mars Odyssey and Instruments.....	5
2.2 Odyssey Thruster Arrangement.....	7
3.1 Odyssey RCS Nozzle Mesh.....	10
3.2 Nozzle Mach Number Contours.....	12
3.3 Nozzle Centerline Mach Number.....	12
3.4 Nozzle Exit Mach Number.....	13
3.5 Aspect Ratio Geometric Variables.....	17
3.6 Nozzle Exit Mesh Converted to Point Sources .....	18
3.7 Plume Number Density Contours, $AF=1.6$ and $DM=0.4$ .....	19
3.8 Iso-density Plume Surface.....	22
4.1 MGS Plume CFD Number Density Contours.....	24
4.2 VNAP MGS Nozzle Mach Number Contours.....	25
4.3 MGS Nozzle Exit Mach Number Comparison Between VNAP and GASP.....	25
4.4 MGS Plume Number Density Contours Using VNAP Exit Properties.....	26
4.5 MGS Plume Number Density Contours Using Isentropic Exit Properties.....	27
4.6 Comparisons of MGS Plume Centerline Number Density.....	28
4.7 MGS Plume Contour Comparison Between Source Flow Code and GASP.....	29
4.8 MGS Plume Centerline Number Density Profiles with Varying Nozzle Boundary Layer Thickness Values.....	31
4.9 MGS Plume Number Density Contour Comparison with Isentropic Nozzle Exit Conditions and Varying Boundary Layer Thickness.....	31
6.1 Nozzle Exit Profile Mach Number for Three Different grid Resolutions.....	38
6.2 Plume Iso-density Contours with Varying $AF$ and $DM$ .....	41
7.1 Odyssey Surface Pressure Contour, No Plumes.....	45
7.2 Odyssey Surface Pressure Contour, RCS-1 Plume.....	47
7.3 Odyssey Surface Pressure Contour, RCS-2 Plume.....	47
7.4 Delta Force Coefficients vs Density, RCS-1.....	55
7.5 Delta Moment Coefficients vs Density, RCS-1.....	55

7.6 Delta Force Coefficients vs Density, RCS-2.....	56
7.7 Delta Moment Coefficients vs Density, RCS-2.....	56
8.1 Attitude Rates Comparison of POST 6-DOF Simulation to Flight Data, Orbit 6, RCS Model Inactive, Thrust Model Active.....	61
8.2 Attitude Comparison of POST 6-DOF Simulation to Flight Data, Orbit 6, RCS Model Inactive, Thrust Model Active.....	62
8.3 Aero Angles Comparison of POST 6-DOF Simulation to Flight Data, Orbit 6, RCS Model Inactive, Thrust Model Active.....	62
8.4 Attitude Rates Comparison of POST 6-DOF Simulation to Flight Data, Orbit 24 RCS Model Active, Thrust Model Active.....	64
8.5 Aero Angles Comparison of POST 6-DOF Simulation to Flight Data, Orbit 24, RCS Model Active, Thrust Model Active.....	65
8.6 Attitude Comparison of POST 6-DOF Simulation to Flight Data, Orbit 24, RCS Model Active, Thrust Model Active.....	65
8.7 Variation of RCS Rolling Moment Coefficient Multipliers with Maximum Density for Orbits 46-100.....	67
8.8 Variation of RCS Rolling Moment Coefficients Multipliers with Maximum Density for Orbits 250-300.....	67

## List of Tables

3.1 Odyssey RCS Nozzle Specifications.....	10
4.1 MGS Nozzle Specifications.....	23
6.1 Aerodynamic Coefficients and Computation Time for DAC Simulations of Odyssey with RCS-2 Active for Varying Grids.....	39
6.2 Aerodynamic Coefficients from DAC Simulations, Plume Model Varying <i>AF</i> and <i>DM</i> , RCS-2 Active.....	42
7.1 Aerodynamic Coefficients for Mars Odyssey with Varying Densities.....	45
7.2 Aerodynamic Coefficients about CM for Mars Odyssey with Plumes.....	46
7.3 Breakdown of RCS Thrust and Aerodynamic Forces.....	48
7.4 RCS-2 Plume Impingement and Flowfield Interaction Effects about CM.....	50
7.5 Superposition of RCS Effects for Multiple Thruster Firings about the CM.....	52
7.6 Conversions from RCS-1 and RCS-2 to RCS-4 and RCS-3.....	54
8.1 Comparing Delta Coefficients to Interpolation Error, RCS-2 Active.....	60

## Nomenclature

A	normalization factor
AF	aspect ratio factor
CAV	coefficient of artificial viscosity
DM	number density multiplier
K	parameter grouping
Kn	Knudsen number
L	characteristic length
Nden	number density
$\dot{N}$	number flow rate
P	Bird breakdown parameter
Q	source term in Boltzmann equation
R	gas constant
SMP	smoothing parameter
T	absolute temperature
d	average molecular diameter
m	species molecular mass
$\hat{n}$	nozzle exit normal
n	number density
p	pressure
$\dot{q}$	energy flux
r	magnitude of x
radp	radius from plume centerline to mesh point
radpos	radius from plume centerline to source grid point
rexit	radius of source
rmag	distance from source grid point to mesh point
s	speed ratio $\equiv \beta u_e$

$u_e$	nozzle exit bulk velocity
$v$	velocity at position $x$
$x$	position
$\Phi$	mass flux
$\beta$	$1/\sqrt{2RT}$
$\delta$	delta function; also, boundary layer thickness
$\lambda$	mean free path
$\theta$	angle measured between $u_e$ and $x$
$\nu$	collision rate
$\rho$	mass density
$\phi$	angle measured between $\hat{n}$ and $x$
$\phi_e$	angle measured between $\hat{n}$ and $u_e$

subscripts:

asy	asymmetric free-molecule source model
j	plume jet
$\infty$	free stream

## Chapter 1. Introduction

NASA's Mars Surveyor Program aims to provide a detailed map of Mars and extensive data on the planet's atmosphere, weather variations, surface, and magnetic field. The first spacecraft of this program was the Mars Global Surveyor (MGS). MGS arrived at Mars in September of 1997 and is still currently in orbit. The next mission in the program consisted of an orbiter and a lander; unfortunately both of them failed. The most recent mission is the Mars Odyssey orbiter. The Odyssey was launched on April 7, 2001 and arrived at Mars on October 23, 2001.

Both Odyssey and MGS utilized a technique known as aerobraking to reduce the spacecraft velocity enough to obtain the desired orbit for scientific research. During aerobraking, a reaction control system (RCS) was used to maintain the desired spacecraft attitude. The RCS consists of multiple thrusters. When the jets from the thruster firings expand into the vacuum of space or a low-density atmosphere, plumes are created that can have inadvertent effects on the spacecraft. The plumes can impinge on the spacecraft and can interact with the flow around the spacecraft thus altering the aerodynamics. Currently, there are rigorous methods to determine the plume effects on spacecraft aerodynamics, but these methods tend to be time intensive and computationally expensive. For this study a quick and relatively accurate model was needed to determine the plume effects. The development and validation of a methodology to model these effects is presented in this report.

Aerobraking takes place in the upper portions of the Martian atmosphere where the flow around the spacecraft is rarefied. In rarefied flow, the assumption of a continuous fluid is no longer valid, so the Navier-Stokes equations no longer hold. Therefore, a simulation method that

accounts for the molecular behavior of the flow is required. One such method is the Direct Simulation Monte Carlo (DSMC) method of Bird<sup>1</sup>. However, the flow inside the RCS nozzle is continuous and can be modeled efficiently using Navier-Stokes or other continuum-based methods. As the flow leaves the nozzle, it transitions from a continuous flow to a rarefied flow. A method is presented for modeling the plume through the transition and extracting a starting surface for DSMC simulations. This method uses an analytical source flow model of the plume expansion and a simple engineering approximation of the continuum to rarefied transition. The method is then applied to the Mars Odyssey to study the effects of RCS firings on the aerodynamics.

The NASA Langley Research Center (LaRC) provided flight mechanics and atmospheric modeling support for the Mars Odyssey during aerobraking. This support required predictions for each orbit of the aerodynamic behavior of Odyssey. The current model was used to develop an aerodynamic database that accounted for the effects of the RCS thrusters plume impingement and plume-flowfield interaction. The application of this model is detailed in this report, along with validation of the method of implementation and comparisons to Odyssey flight data.

Overall, the following steps summarize the methodology used to determine the plume effects on the Mars Odyssey during aerobraking.

- 1) Create the nozzle geometry and use a computational fluid dynamics (CFD) program to determine the internal nozzle flow and the nozzle exit plane properties.
- 2) Use a source flow program to determine the plume flowfield and extract inflow conditions for the DSMC simulations.

- 3) Utilize DSMC to model the flow and to determine the change in aerodynamic coefficients on the Odyssey caused by the plumes.
- 4) Incorporate the aerodynamic changes into a 6-DOF simulation of Odyssey during aerobraking.

## Chapter 2. Mars Odyssey Mission

### 2.1 Objectives

The 2001 Mars Odyssey is an orbiting spacecraft carrying three scientific instruments designed to make global observations of Mars to improve our understanding of the planet's climate and geologic history, including the search for liquid water and evidence of past life<sup>2</sup>. Odyssey's primary mission is to map the chemical elements and minerals in the Martian surface, determine the amount of hydrogen in the shallow subsurface, and analyze the Martian near-space radiation environment. A secondary mission will be to provide a communications link with future Mars missions. The three instruments attached to the orbiter to achieve the primary goals are the Thermal Emission Imaging System (THEMIS), the Gamma Ray Spectrometer (GRS), and the Mars Radiation Environment Experiment (MARIE). The GRS includes the Gamma Sensor Head and the High Energy Neutron Detector. **Figure 2.1** shows the Mars Odyssey along with labels pointing to these instruments.

THEMIS relies on thermal infrared spectroscopy to identify rocks and minerals. While orbiting Mars, THEMIS will search for regions of the surface that resemble hydrothermal or sub-aqueous environments by determining the mineralogy and searching for temperature anomalies. The GRS will determine the elemental abundances in the Martian surface and try to determine the presence of water near the surface, the depth of the polar ice caps, and the polar ice caps variation with time. The GRS will also gather information on cosmic gamma-ray bursts. The MARIE will determine the radiation environment at Mars.

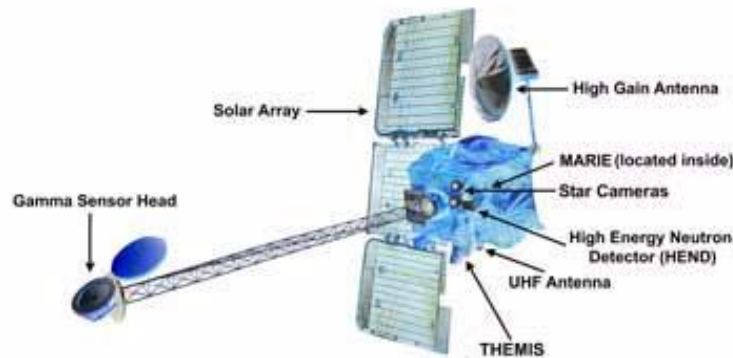


**Figure 2.1.** Mars Odyssey and Instruments

## **2.2 Aerobraking**

When Odyssey reached Mars on October 23, 2001, a Mars orbit insertion (MOI) maneuver was performed. During the MOI, the main engine was fired to reduce the velocity enough for the spacecraft to be captured by Mars' gravity. The Odyssey was initially in approximately an 18.6-hour elliptical orbit. Aerobraking was used to further reduce the spacecraft velocity, thus reducing the orbit to the circular 2-hour science orbit desired. Aerobraking is a process where a spacecraft dips into the upper portions of an atmosphere to allow the aerodynamic drag to reduce the velocity of the spacecraft. Previous missions that did not utilize aerobraking relied on thruster firings to reduce the spacecraft velocity. Using the atmospheric drag force to slow a spacecraft instead of thruster firings reduces the amount of fuel necessary to obtain the desired orbit. Aerobraking is usually performed over a long period of time

as the orbit is gradually reduced through a large number of passes through the upper atmosphere. Dipping a spacecraft deeper into the atmosphere can reduce the aerobraking time, but also increases the forces and the heating on the spacecraft. Structural and thermal limits provide a constraint on how deep into the atmosphere the spacecraft can safely penetrate, and thus on how quickly aerobraking can be performed. For the Odyssey, aerobraking took 75 days using a total of 336 passes.

The Mars Odyssey is the third mission to use aerobraking, and only the second mission to rely on aerobraking to reduce its orbit upon arrival to a planet. The first mission to rely on aerobraking during the arrival was the Mars Global Surveyor (MGS) in 1997. MGS successfully performed aerobraking to reduce and circularize its orbit even though it had a broken latch on one of the solar panels. The broken latch resulted in the aerobraking taking approximately eight months longer than originally anticipated. Aerobraking was first tested during the Magellan mission to Venus in September of 1994. After Magellan's primary mission was complete, the Windmill Experiment was performed. The orbit was lowered and the solar panels were turned to resemble blades of a windmill; then flight controllers measured how much control torque was necessary to maintain attitude and keep the spacecraft from spinning. The Windmill Experiment helped scientists observe the aerodynamic behavior in the upper atmosphere and laid the groundwork for future aerobraking.

During aerobraking, Odyssey's attitude was controlled by a reaction control system (RCS). The RCS for the Mars Odyssey includes four 0.2 lbf thrusters. The thrusters are canted so that they are not aligned with the mechanical axes, which allow the four thrusters to provide three-axis control. The thruster arrangement is shown in [Figure 2.2](#). Also shown in the figure are four

TCM thrusters. These thrusters are primarily used for orbit maneuvers and serve as a backup to the RCS thrusters during aerobraking passes.

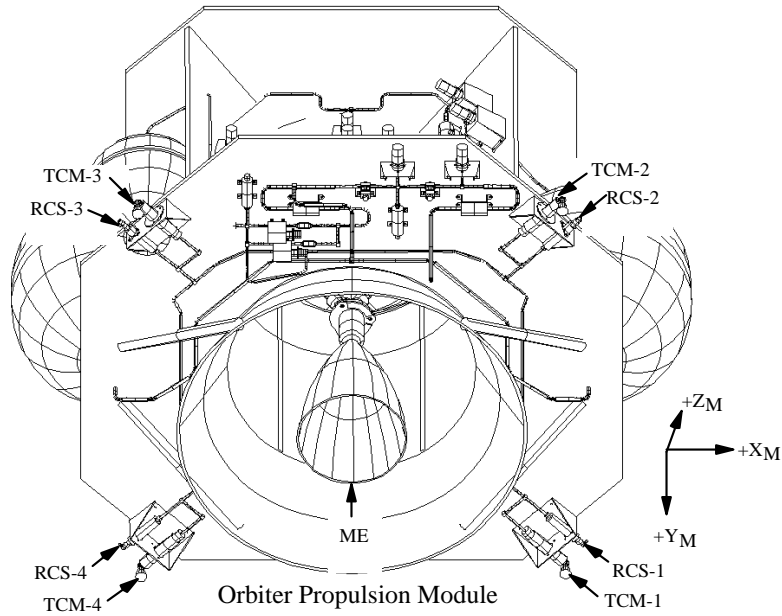


**Figure 2.2.** Odyssey Thruster Arrangement

## Chapter 3. Development of a Source Flow Plume Model

In previous studies on MGS aerodynamics, RCS plumes were predicted to cause significant interaction effects<sup>3</sup>. For MGS, the plume effects decreased the drag by up to 15% and changed the yaw and pitch moments. In some instances, the moments caused by the plume effects were greater than the moments due to the thrust, and in the opposite direction. This resulted in “thrust reversal” where the total moment due to a thruster firing was in the opposite direction of that intended. The thrust reversal shown in the MGS study was a motivating factor to perform the present study of the Odyssey plume effects.

To perform a study of RCS plume effects on the Odyssey, it was important to have a model that could accurately predict the plume characteristics. A plume can be difficult to simulate since the flow typically extends from continuum near the nozzle and then passes through the transition regime before becoming free-molecule flow. In a near vacuum, this expansion occurs within a relatively short distance from the nozzle exit. Since all of the Odyssey RCS thrusters are identical, a plume flowfield calculated for one could be used for the others as well. There are a variety of methods currently used to approximate plume flowfield characteristics. Some of these methods include; point source, method of characteristics, distributed source flow, and codes utilizing the Navier-Stokes equations. For the purpose of this research, it was necessary to develop or determine a method that could be used both quickly and accurately to model the plume. It was also desired to have a plume model that was relatively general and could be used quickly for different thrusters under varying conditions with minimal alterations.

A point source model assumes the flowfield can be modeled by a single point source at the nozzle exit location. The properties of the point are based on the average properties of the nozzle exit. This method is very fast computationally, but loses accuracy due to the averaging at the nozzle exit. Information such as variations in flow properties across the boundary layer is lost. To retain more detailed nozzle exit properties, many point source models can be used together forming a distributed source flow model<sup>3</sup>. A distributed source flow model is still relatively fast computationally, but has the added information of local nozzle exit properties. CFD codes also use the local nozzle exit properties, but CFD codes tend to be computationally expensive and since they are based on continuous flow, they lose accuracy as the flow expands into the low-density atmosphere where the Navier-Stokes equations are no longer accurate.

The plume model used in the present study is based on source flow principles and was devised by Woronowicz<sup>4</sup>. The model was chosen based on the small computation time and prior studies which indicated the model would provide the needed accuracy<sup>4</sup>. Since the model requires the nozzle exit plane properties, it was necessary to separately determine the internal nozzle flow.

### **3.1 Internal Nozzle Flow Calculation**

The internal nozzle flow was computed using a CFD program called VNAP (Viscous Nozzle Analysis Program)<sup>5</sup>. VNAP uses a second-order accurate finite difference scheme to solve the Navier-Stokes equations for two-dimensional, time dependent, compressible flow. VNAP assumes the fluid is a perfect gas. Unlike the flowfield of the plume, the flow in the nozzle is continuous and can be modeled accurately with the Navier-Stokes equations. The 2-D

axisymmetric geometry for one of the RCS thrusters was created using information about the thrusters listed in [Table 3.1](#). The nozzle geometry upstream of the throat was approximated for the purpose of the CFD run. A grid was developed for the nozzle geometry concentrating the points around the throat and in the boundary layer. It was necessary to ensure that there was a grid point exactly at the throat of the nozzle so that the effective area ratio was correct. The final grid is shown in [Figure 3.1](#). A calculation of the Reynolds number based on the throat conditions determined a Reynolds number of 62, which implies the internal flow should be laminar.

**Table 3.1.** Odyssey RCS Nozzle Specifications

Thrust	0.8896 N
Exit Radius	0.29 cm
Area Ratio	100:1
Chamber Pressure	2.034 MPa
Chamber Temperature	1166.7 K
Exit Half Angle	15 degrees
Exit Mach Number	6.41

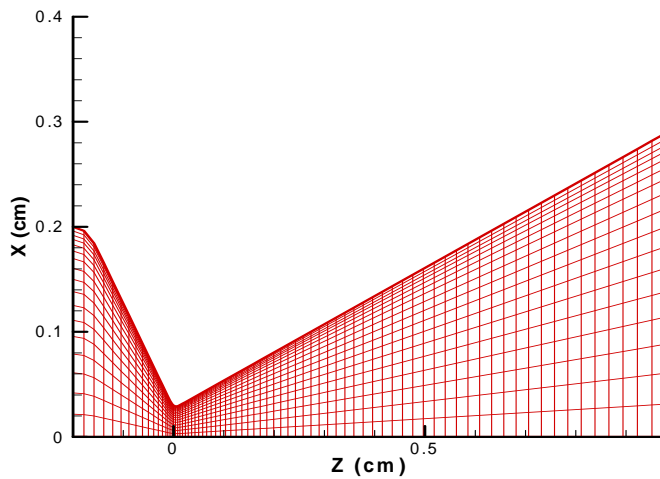


**Figure 3.1.** Odyssey RCS Nozzle Mesh

With the physical values set, there are also some key computational parameters that VNAP allows the user to adjust to obtain accurate results for the run. Three variables in particular were studied; number of time steps, coefficient of artificial viscosity (CAV), and a smoothing parameter (SMP). The number of time steps chosen must be enough to achieve steady state. CAV multiplies finite difference viscosity terms (default is 0.0) and is used mainly in the region of shocks. SMP is applied during the initial transient stage of the simulation to control numerical instabilities (default is 0.95).

The first parameter studied was the number of time steps. The Mach number was chosen as reference variable because the manufacturer of the thrusters provided a maximum exit Mach number of 6.41. This value is not input into VNAP and can serve as a check to see if the simulation gives approximately the same maximum Mach number at the exit. The simulation was performed for 1000, 2000, 3000, 4000, and 5000 time steps. The exit Mach number profiles were compared to determine steady state. 4000 time steps achieved steady state; further increases in the number of time steps had no significant change in the Mach number profile.

Simulations using CAV values of 0.05, 0.1, and 0.15 proved to have no detectable effect on the results. A CAV of 0.1 was chosen for the remainder of the simulations. With a high SMP value (0.95), which correlates to little smoothing during the transient period, there was a spike in the Mach number distribution near the throat. The spike could possibly represent a weak shock in the nozzle. Decreasing the SMP, thus increasing the smoothing, reduced the shock but resulted in a thicker boundary layer with a wavy shape. The SMP was set to the value of 0.8 that proved to reduce the shock near the throat while maintaining a smooth and relatively thin boundary layer.

Using the above values, a final run was performed to determine the nozzle exit properties. A contour of the Mach number in the nozzle is shown in **Figure 3.2**. **Figure 3.3** shows the Mach number along the nozzle centerline. The spike seen at approximately 0.1 cm is the spike referred to previously that could be a weak internal shock. The maximum Mach number at the nozzle exit is approximately 6.27. This value is close to the manufacturer's defined maximum value of 6.41.

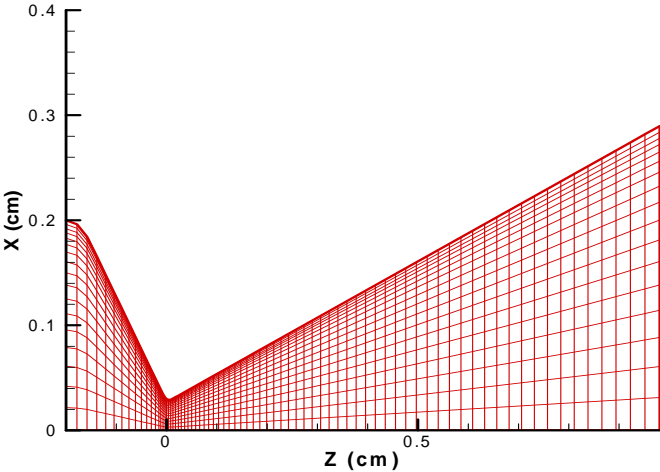


**Figure 3.2.** Nozzle Mach Number Contours

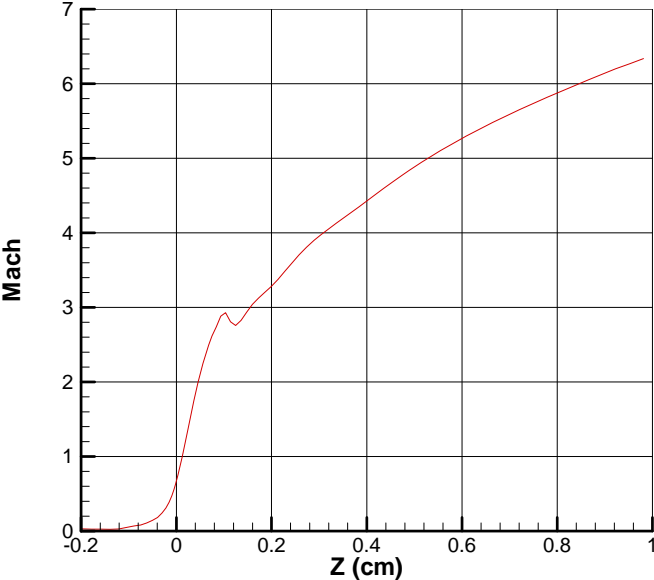


**Figure 3.3.** Nozzle Centerline Mach Number

The nozzle exit properties are given along a 1-D line from the centerline of the nozzle to the nozzle wall. The Mach number profile at the nozzle exit is shown in **Figure 3.4**. Using the assumption that the flow at the exit is symmetric, the solution along the line was propagated 360° about the centerline to form a 2-D exit plane solution, which was the input into the source flow model.

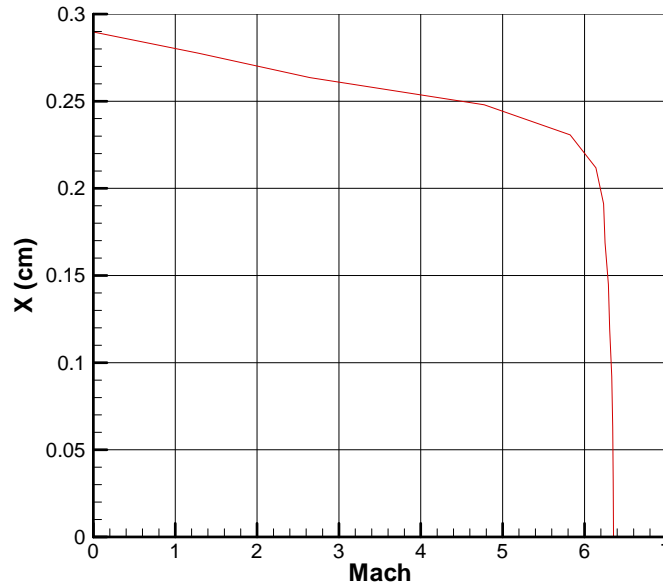


**Figure 3.4.** Nozzle Exit Mach Number

### 3.2 Theory of the Source Flow Model

Source flow models are basically spatial distribution functions for plume flowfield properties derived from conservation of mass and energy<sup>6</sup>. The Woronowicz model divides the exit plane into many point sources. Each point represents a small section of the nozzle exit and has properties based on the local flow in the nozzle. In the current implementation, an arbitrary plume mesh is created downstream of the nozzle exit. The flowfield contributions at each point in

the mesh are calculated for each individual point source, and the results are summed to get the total influence of the sources on the flow properties at each mesh point.

Once the basic geometric relationships between the nozzle exit mesh and the plume mesh have been determined, the plume flowfield can be calculated. The model developed by Woronowicz uses free-molecular theory to describe the flowfield. Assuming that the flow expands radially from each point source, properties at each mesh point can be calculated using the conservation equations. A source term  $Q$  was developed for a time-dependent solution of the collisionless Boltzmann equation. The  $Q$  equation is given below.

$$Q = \frac{2\beta^4}{A\pi} \delta(x) \dot{N}(t) \left| \mathbf{v} \cdot \hat{\mathbf{n}} \right| \exp(-\beta(v - u_e)^2) \quad (1)$$

Where  $A$  is a normalization factor calculated by,

$$A = e^{-s^2 \cos^2 \phi_e} + s\sqrt{\pi} \cos \phi_e (1 + \text{erf}(s \cos \phi_e)) \quad (2)$$

The number density in the flowfield is computed at steady state by the equation,

$$n(x) = \frac{\beta \dot{N} \cos \phi}{A\pi r^2} e^{-s^2 \sin^2 \theta} \{ (s \cos \theta) \exp(-s^2 \cos^2 \theta) + (1/2 + s^2 \cos^2 \theta) \sqrt{\pi} (1 + \text{erf}(s \cos \theta)) \} \quad (3)$$

Then, the following equations<sup>4</sup> are used to obtain mass flux  $\Phi$ , pressure  $p$ , and translational energy flux  $\dot{q}$ :

$$\Phi(x) = K_{asy} \frac{x}{r} \left\{ (1 + s^2 \cos^2 \theta) \exp(-s^2 \cos^2 \theta) + \left( \frac{3}{2} + s^2 \cos^2 \theta \right) \sqrt{\pi} (s \cos \theta) (1 + \text{erf}(s \cos \theta)) \right\} \quad (4)$$

$$p(x) = \frac{K_{asy}}{\beta} \left\{ \left( \frac{5}{2} s \cos \theta + s^3 \cos^3 \theta \right) \exp(-s^2 \cos^2 \theta) + \left( \frac{3}{4} + 3s^2 \cos^2 \theta + s^4 \cos^4 \theta \right) \sqrt{\pi} (1 + \operatorname{erf}(s \cos \theta)) \right\} \quad (5)$$

$$\dot{q}(x) = \frac{K_{asy}}{2\beta^2} \frac{x}{r} \left\{ \left( 2 + \frac{9}{2} s^2 \cos^2 \theta + s^4 \cos^4 \theta \right) \exp(-s^2 \cos^2 \theta) + \left( \frac{15}{4} + 5s^2 \cos^2 \theta + s^4 \cos^4 \theta \right) \sqrt{\pi} (s \cos \theta) (1 + \operatorname{erf}(s \cos \theta)) \right\} \quad (6)$$

where  $\rho = mn(\mathbf{x})$ , and

$$K_{asy} = \frac{m \dot{N} \cos \phi}{A \pi r^2} e^{-s^2 \sin^2 \theta} \quad (7)$$

With these terms defined, the velocity and translational temperature can also be determined in the flowfield using the equations:

$$v(x) = \frac{\dot{\Phi}(x)}{\rho(x)} \quad (8)$$

$$T(x) = \frac{1}{3R} \left\{ \frac{p(x)}{\rho(x)} - (v(x))^2 \right\} \quad (9)$$

Although the free-molecular description of the flow is not valid in the continuum core of the plume, it has been found that the radial expansion assumption gives a reasonably accurate approximation of the spatial variations in plume flow properties at sufficiently large distances from the exit. Furthermore, the free-molecular conservation formulation has been shown to capture much of the functional dependence of these properties on nozzle exit conditions<sup>4</sup>.

Empirically derived corrections can then be made to account for nonlinear behaviors caused by phenomena such as plume shocks and boundary-layer expansion<sup>6</sup>.

The plume model was previously modified to have two adjustable parameters to allow the user to calibrate the model. The first parameter,  $AF$ , controls the plume's aspect ratio. Increasing the aspect ratio factor creates wider plumes and decreasing the factor creates slimmer plumes while maintaining the same centerline properties. In the plume model, the aspect ratio factor is applied only when the radius from the plume centerline to the plume mesh point,  $radp$ , is greater than the radius from the plume centerline to the source grid point,  $radpos$ , and the distance from the source grid point to the plume mesh point;

$$rmag = \sqrt{\Delta x^2 + \Delta y^2 + \Delta z^2} \quad (10)$$

is greater than the radius of the source itself,  $rexit$ . The geometric variables are shown in **Figure 3.5**. When these conditions are satisfied, a new  $rmag$  is calculated using values determined by the equations,

$$\Delta x = \Delta x / AF \quad (11)$$

$$\Delta y = \Delta y / AF \quad (12)$$

The results from the previous free molecule equations listed above are then shifted based on the new  $rmag$  value.

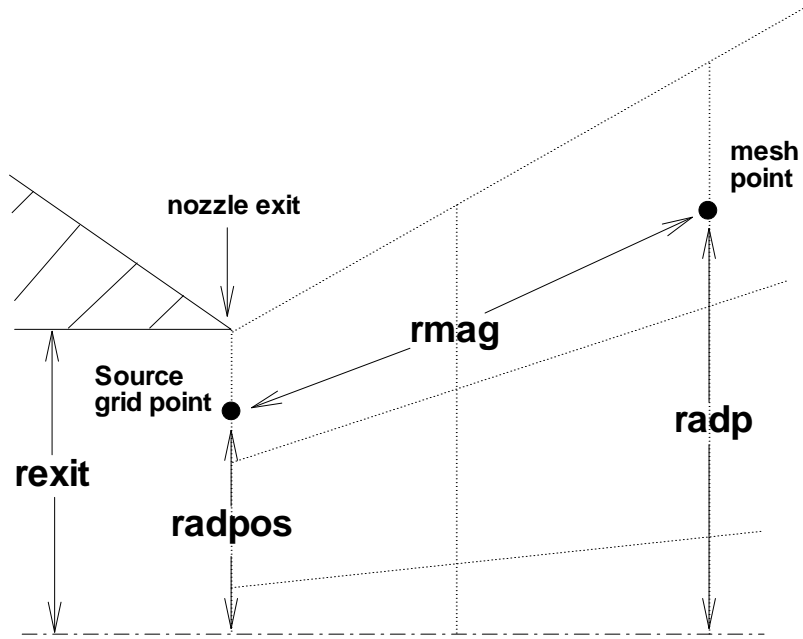


**Figure 3.5.** Aspect Ratio Geometric Variables

The second parameter is a number density multiplier,  $DM$ . This parameter uniformly multiplies the number density in the plume flowfield by a constant value, as shown in the equation below,

$$N_{den} = DM * N_{den} \quad (13)$$

The baseline value chosen for the aspect ratio parameter is 1.6 and the value chosen for the number density multiplier is 0.4. These values were determined in previous calibrations with CFD results for unpublished work. These parameters may be adjusted as needed where other plume data is available to better represent a particular plume.

### **3.3 Modification made to the source flow model**

The nozzle exit plane data was reformatted for the source flow model by creating a triangulated mesh in which each of the four-sided elements was bisected to form two triangles

(see [Figure 3.6](#)). The point source properties of each triangle were based on its area and on the average property values at each of the three vertexes composing the triangle.

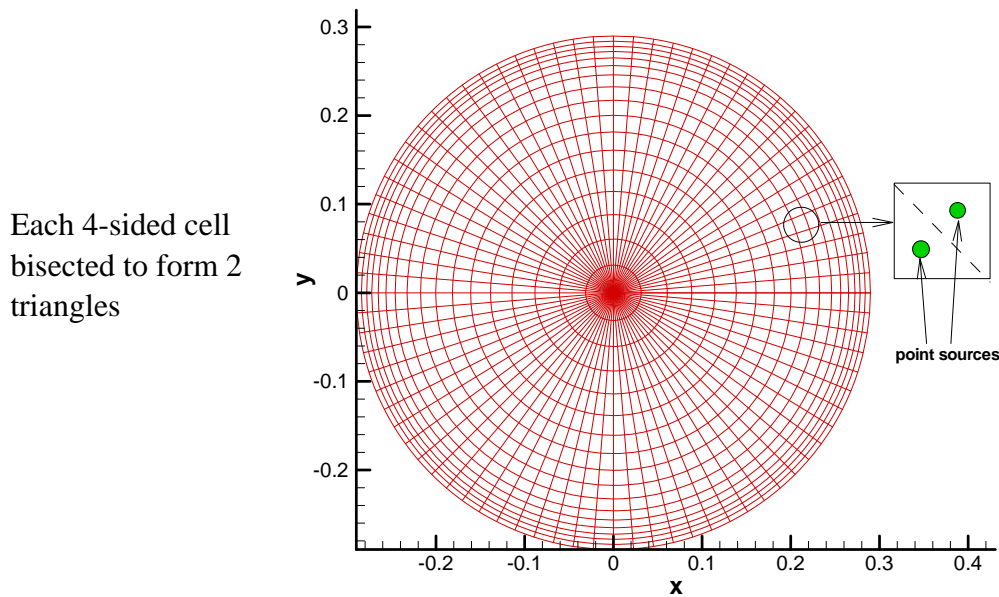


**Figure 3.6.** Nozzle Exit Mesh Converted to Point Sources

The original source flow model placed a three-dimensional plume mesh above the nozzle exit plane solution. Then the flowfield properties were calculated for each point in the plume mesh as described previously. In an effort to reduce the computation time needed, the program was modified to use a two-dimensional axisymmetric plume mesh, which could then be revolved around the axis to form the three-dimensional plume flowfield. The plume mesh size is determined by the size of the nozzle exit and two variables that allow the user to adjust the plume mesh if needed. Once the plume mesh is created the actual source flow program described in the previous section is run to determine the plume flowfield. The number density contours of the plume flowfield are shown in [Figure 3.7](#) for the nominal values chosen for the aspect ratio and density multiplier parameters.

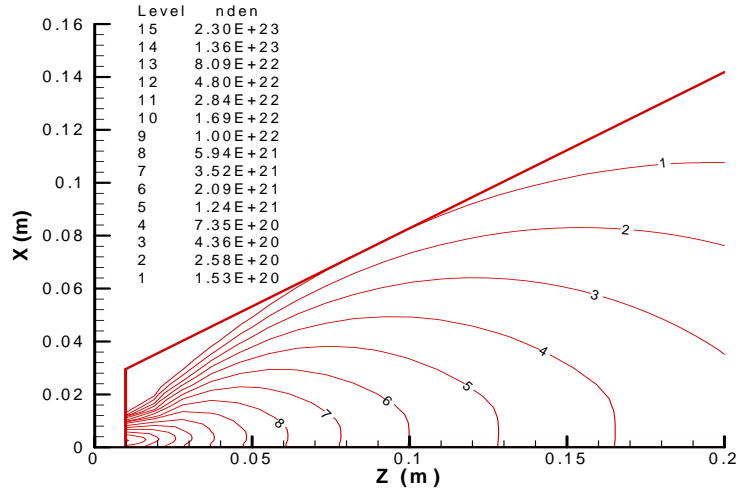


**Figure 3.7.** Plume Number Density Contours,  $AF=1.6$  and  $DM=0.4$

Once the plume flowfield is defined, a boundary surface must be extracted to provide a set of inflow conditions for the DSMC calculations. The boundary between continuum and transitional flow that is used for DSMC simulations is often determined based on the Bird breakdown parameter<sup>1</sup>,  $P$ , which relates the collision length scale to the gradient length scale for density expansion. The Bird breakdown parameter can be expressed as

$$P = (1/v) * |D(\ln \rho)/Dt| \quad (14)$$

where  $v$  is the collision frequency. This approach was used in the work of Glass<sup>7</sup>, which used a full Navier-Stokes CFD computation for the continuum portion of the RCS plume for MGS. For  $P > 0.02$ , the flow departs from continuum theory because the collision frequency is too low to maintain local thermal equilibrium. With the current simple flow model, the source flow theory does not capture the detailed density gradients in the continuum portion of the plume, and computation of the Bird breakdown parameter from the flowfield is likely to produce significant errors. Since the objective of the current work is to capture the first-order plume impingement

and flowfield interaction effects, an alternate scheme was chosen that is expected to satisfy these objectives.

To create a surface for the DSMC simulations, an iso-density surface was chosen based on the momentum ratio of the plume to the free stream flow;

$$\frac{\rho_j v_j^2}{\rho_\infty v_\infty^2} \quad (15)$$

The plume surface will be modeled as an out-gassing surface in DSMC, that is particles which flow out of the surface become part of the simulation while particles that flow into the surface are removed from the simulation. Therefore the momentum ratio has to be high enough that only a negligible number of atmosphere particles can penetrate the plume. If the ratio is too low, the amount of particles penetrating the plume will no longer be negligible and error will be introduced into the calculations. Higher values for the ratio produce smaller iso-density surfaces. The source flow model is not accurate until approximately 10 nozzle diameters down the plume centerline, which implies that the momentum ratio should not be high enough to create a plume iso-density surface that is closer to the nozzle than 10 nozzle diameters on the centerline.

A momentum ratio of 100 was found to satisfy these requirements and this value was chosen to guide the selection of an appropriate boundary between continuum and transitional flow. In principle, an inflow surface could be determined based on a constant value for the momentum ratio. However, the presence of the boundary layer, where the velocity approaches zero, produces large gradients in velocity near the nozzle lip and make the definition of an iso-momentum ratio surface very difficult in this region. Since the plume velocity approaches a constant limit fairly rapidly as the plume expands, the momentum ratio can be approximated by

$$\frac{\rho_j v_j^2}{\rho_\infty v_\infty^2} \rightarrow Const * \left( \frac{\rho_j}{\rho_\infty} \right) \quad (16)$$

at large distances from the exit. Therefore, an iso-density surface can be defined which approximates the chosen momentum ratio at large distances and provides a more well behaved surface shape near the exit. The iso-density approximation was used to define the plume surface for the DSMC part of this study.

To create the iso-density surface, the program first determines an iso-density line in the 2-D flowfield. Once the iso-density line has been determined, it is rotated about the centerline of the plume to create an iso-density surface. The surface is triangulated in a similar manner described previously. An end cap is added to the plume surface at the nozzle exit to create a “watertight” surface, or a surface that has no holes in it. The end cap is given a different boundary condition than the rest of the surface since the end cap represents flow into the continuum region of the plume which is excluded from the DSMC calculation. Finally, the complete surface is converted into a format that is compatible with the DSMC program. A typical iso-density plume surface is shown in [Figure 3.8](#).

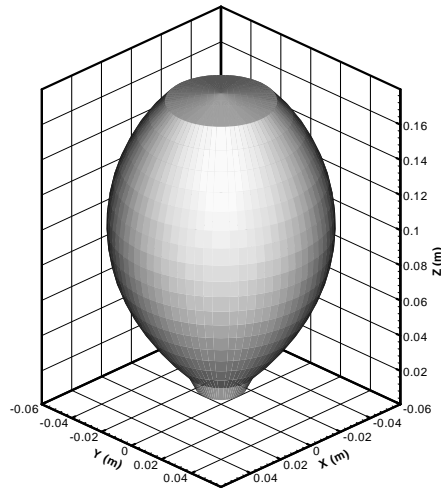


**Figure 3.8.** Iso-density Plume Surface, Momentum Ratio =100,  $\rho_{den}=6.1 \times 10^{20} /m^3$

## Chapter 4. Plume Model Validation

The original source flow model by Woronowicz has been compared to other engineering models and to CFD plume predictions with satisfactory results<sup>4</sup>. It has also had limited use in practical problems such as predicting plumes for the X-37. The original model has undergone significant changes as detailed earlier in this report, and it is necessary to validate the modified source flow model to provide confidence in the results.

### 4.1 MGS Comparison

Since CFD results were available for an MGS thruster, which has similar characteristics to the Odyssey thruster, the MGS plume was selected to validate the current source flow model.

Table 4.1 lists the nozzle properties for the MGS thruster.

**Table 4.1:** MGS Nozzle Specifications

Thrust	3.0 N
Exit Radius	0.7633 cm
Area Ratio	75:1
Chamber Pressure	1.90133 Mpa
Chamber Temperature	1166.7 K
Exit Half Angle	15 degrees

The MGS nozzle is similar to the Odyssey nozzle, so the plume flowfields should be similar. Both of the thrusters use monopropellant hydrazine. Extensive analysis of the MGS plume flowfield has previously been performed by Glass<sup>7</sup>. Glass utilized the CFD program GASP (The

General Aerodynamic Simulation Program) to simulate the flowfield and to define the plume breakdown surface. The breakdown surface was defined by a Bird breakdown parameter value of  $P = 0.02$ . When  $P > 0.02$ , the expanding flow is not in thermal equilibrium and is not adequately defined by a continuum CFD analysis<sup>7</sup>. The contours of number density for the plume as obtained by Glass are shown in Figure 4.1. As seen from these contours, the CFD simulation included both the internal nozzle flow and the external flow.

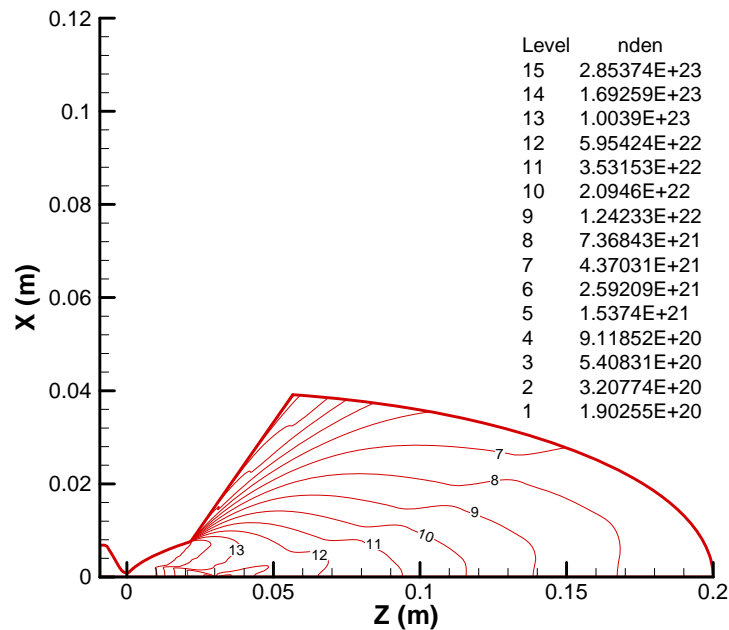


**Figure 4.1.** MGS Plume CFD Number Density Contours

To begin the comparison, first the internal nozzle flow was calculated, again using VNAP as described previously. The Mach number contours are shown in Figure 4.2. Since it is the nozzle exit plane that is input into the source flow program, the properties along this plane are compared to the properties along the same plane from the Glass results. A comparison of the exit plane Mach number is shown in Figure 4.3. The exit profiles are similar but the GASP results

consistently display a higher Mach number. There is an increase in the Mach number near the nozzle symmetry line for both cases.

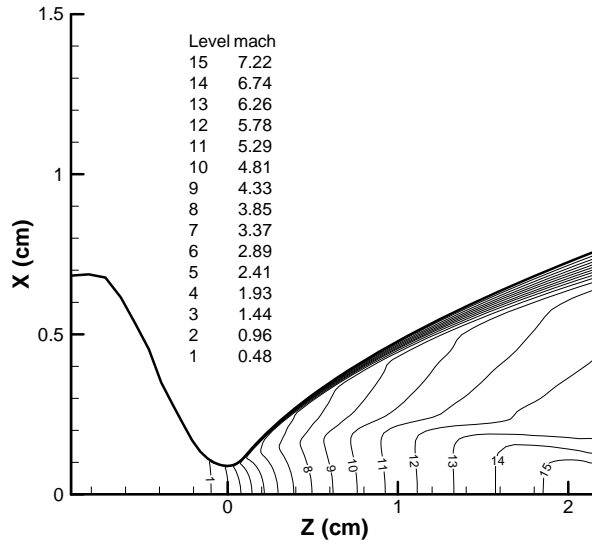
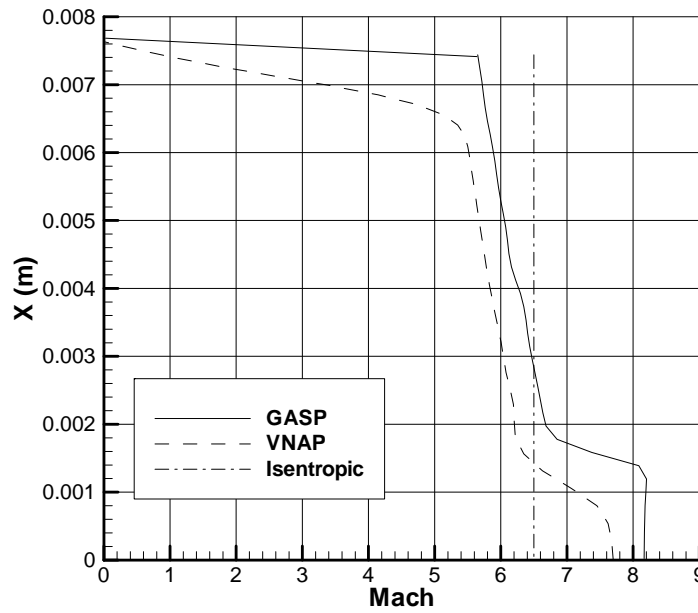


**Figure 4.2.** VNAP MGS Nozzle Mach Number



Contours

**Figure 4.3.** MGS Nozzle Exit Mach Number Profile Comparison Between VNAP and GASP

This increase is caused by an internal shock in the nozzle. The wall boundary layer is also thicker for the VNAP results. The Mach number exit profile for an isentropic nozzle is also included in the figure. The isentropic case was included in the comparison to determine if using detailed internal nozzle flow properties for input into the source flow code resulted in a more accurate plume flowfield prediction.

Using the exit plane information from VNAP, the source flow program was used to generate the plume flowfield. For this comparison, the attenuation factor was set to 1.0 and the density multiplier was set to 0.7. These values improved the comparison between the source flow code results and the GASP results. Number density contours of the flowfield are shown in

Figure 4.4.

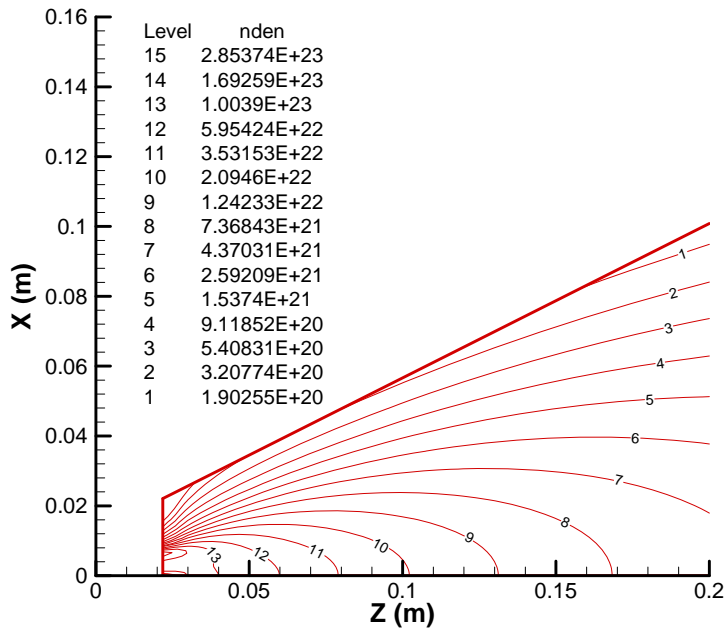
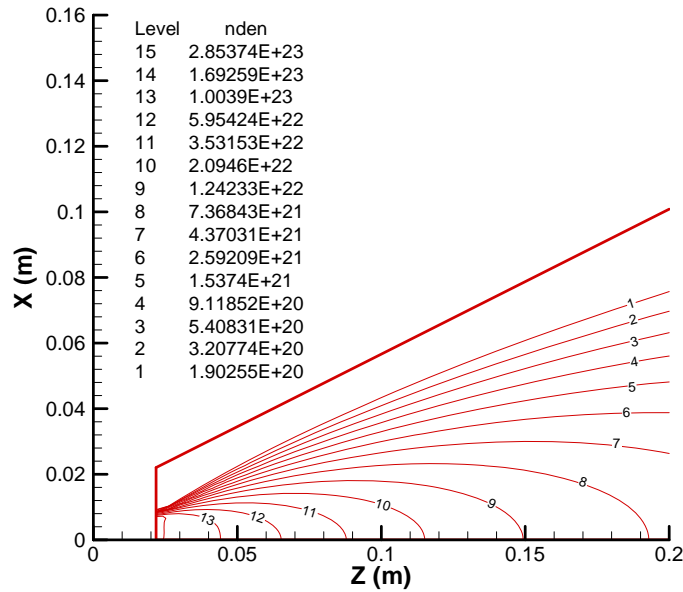


Figure 4.4. MGS Plume Number Density Contours Determined by the Source Flow Code Using VNAP Nozzle Exit Properties

A plume flowfield was also generated using the isentropic nozzle exit conditions. The number density contours of this flowfield are shown in [Figure 4.5](#).



**Figure 4.5.** MGS Plume Number Density Contours Determined by the Source Flow Code Using Isentropic Nozzle Exit Properties

[Figure 4.6](#) compares the number density along the plume centerline for the GASP results and for the source flow program results using both the VNAP solution and the isentropic solution for the nozzle exit. The results match well except for in the proximity of the nozzle exit, where the source flow program is not considered accurate. For the Glass results, there is a reflected shock in the flowfield due to the internal shock in the nozzle. The reflected shock is not present in the source flow plume flowfield since a source flow model cannot model shocks. The Glass results also show a flowfield that is slightly more elongated than the source flow plume flowfield. An individual number density contour line ( $nden = 2.0946E+22$ ) from the GASP results is compared to the same number density contour line from the source flow program results in [Figure 4.7](#).

Again, the isentropic case is also included for comparison. The elongation in the GASP results is most likely due to the reflected shock. From these comparisons, it can be concluded that the GASP results and the source flow results using the VNAP solution show good correlation. The source flow results with the isentropic nozzle exit solution also correlated well with the other results.

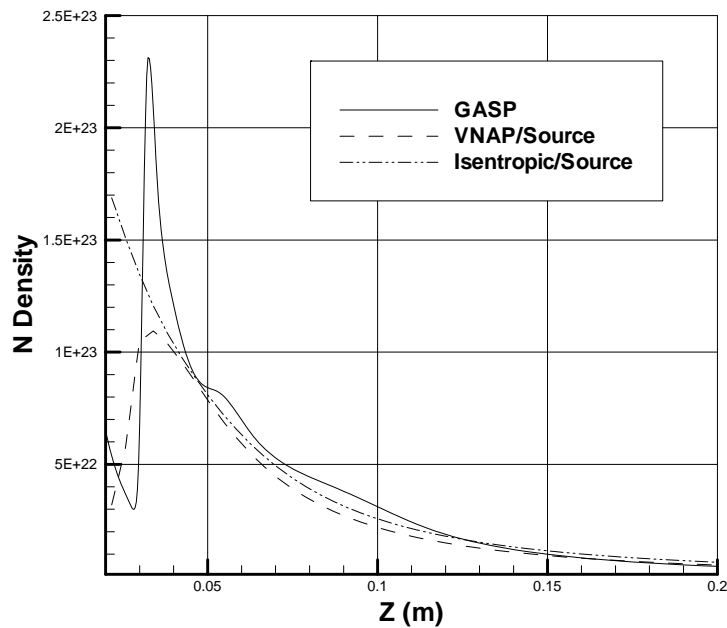


**Figure 4.6.** Comparison of MGS Plume Centerline Number Density Between the Source Flow Code and GASP

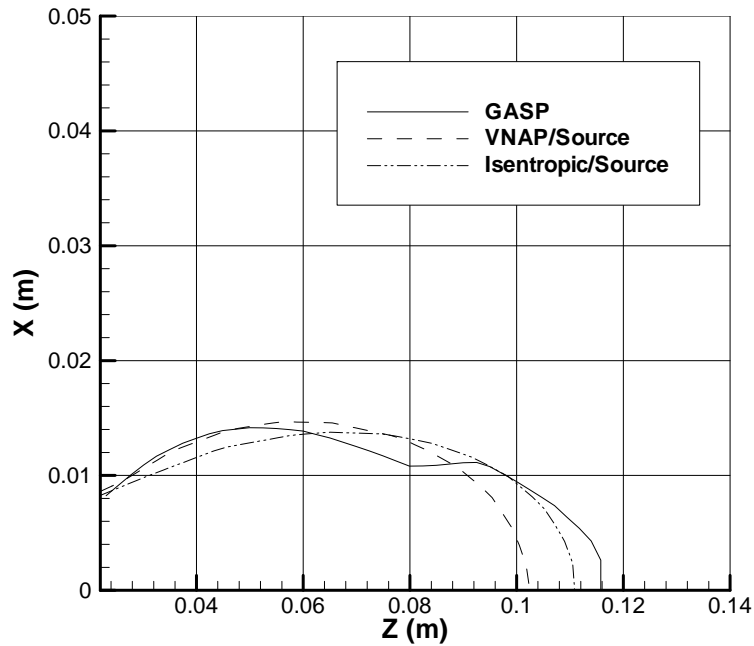


**Figure 4.7.** MGS Plume Number Density Contour Comparison Between the Source Flow Code and GASP,  $nden = 2.0946E+22$

## 4.2 Boundary Layer Sensitivity

To assess the sensitivity of the plume flowfield to the boundary layer developed inside the nozzle, boundary layers of varying arbitrary thickness were added to the isentropic nozzle exit properties. The MGS nozzle was used for this comparison since isentropic nozzle exit properties had already been determined and discussed previously for this nozzle. The pressure was held constant throughout the boundary layer and the temperature varied linearly from the isentropic temperature at the exit to the wall temperature. The velocity in the radial direction varied according to the equation,

$$V = V_{mag} \left( \frac{y}{\delta} \right)^{\frac{1}{7}} \quad (17)$$

where  $V_{mag}$  is the magnitude of the velocity at the exit of the nozzle,  $y$  is the distance from the nozzle wall and  $\delta$  is the boundary layer thickness. Three  $\delta$  values were chosen for the comparison; 0.0643, 0.1385, and 0.2225 cm.

The source flow program was run to calculate the plume flowfields using the isentropic nozzle exit conditions with each of the three boundary layer thickness values. The plume centerline number densities for the three cases are compared to each other and to the results without the boundary layer in [Figure 4.8](#). Near the nozzle exit no effect is evident, but as the distance from the nozzle exit increases, the plume centerline number density decreases for increasing boundary layer thickness. [Figure 4.9](#) was included to show a comparison of a single contour line for each of the cases. The contour lines represent a constant number density of  $2.0946E22$  molecules/m<sup>3</sup>. Increasing the boundary layer thickness results in a smaller plume. This is expected since increasing the boundary layer thickness effectively reduces the mass flow exiting the nozzle.

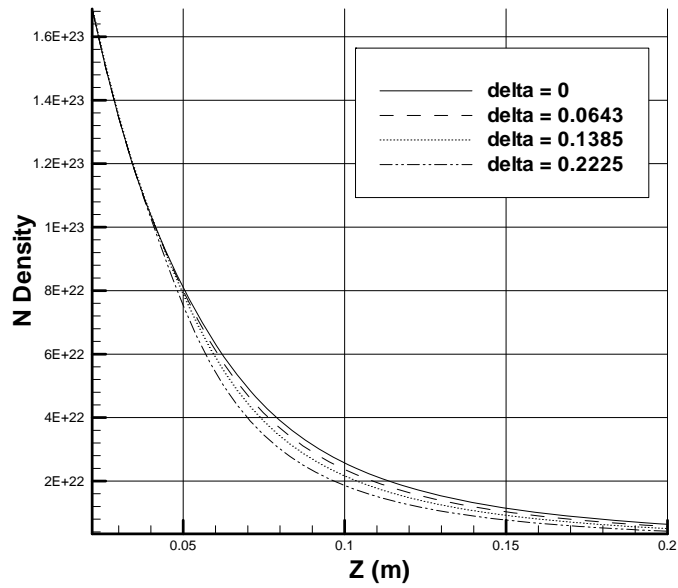


**Figure 4.8.** MGS Plume Centerline Number Density Profiles with Varying Nozzle Boundary Layer Thickness Values

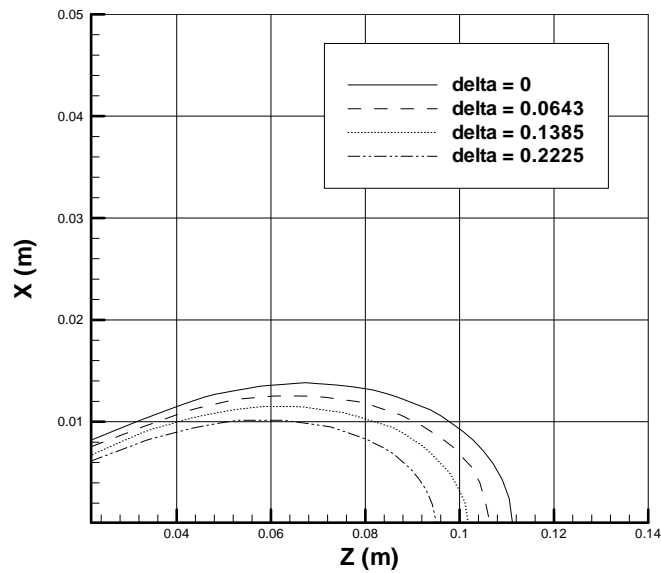


**Figure 4.9.** MGS Plume Number Density Contour Comparison with Isentropic Nozzle Exit Conditions and Varying Boundary Layer Thickness,  $nden = 2.0946 \times 10^{22}$

## Chapter 5. Plume-Flowfield Interaction Modeling

The Mars 2001 Odyssey RCS thrusters were used primarily during aerobraking in a portion of the atmosphere where the flow about the vehicle is highly rarefied. To accurately simulate the interactions, it was necessary to understand characteristics of rarefied flow and of the computer program that was used to simulate the flow.

### 5.1 Rarefied Flow

Rarefied flow occurs when the distance traveled by molecules between collisions is comparable to some characteristic dimension of the problem and is usually divided into two flow regimes; free molecular and transitional. The difference between these two flow regimes is the degree to which these collisions affect the flow properties. The *mean free path* ( $\lambda$ ) is the average distance a molecule travels before a collision with another molecule. As the density of a gas decreases, the mean free path increases since there are fewer molecules with which to collide. The mean free path in an equilibrium gas of hard sphere molecules is given by,

$$\lambda = \left( \sqrt{2} \pi d^2 n \right)^{-1} \quad (18)$$

where  $d$  represents the average molecular diameter and  $n$  represents the local number density of the gas<sup>1</sup>.

The Knudsen number (Kn) is the ratio of the mean free path to a characteristic length, given by,

$$\text{Kn} = \lambda/L \quad (19)$$

The Knudsen number can be used to characterize the flow regime. As the density of a gas decreases, the mean free path will increase and the Knudsen number will also increase. Thus,

larger Knudsen numbers represent a rarefied flow. Typically,  $Kn > 10$  is considered free molecular flow and  $0.1 < Kn < 10$  is considered transitional flow. In both regimes, the molecules will give up a fraction of energy and momentum upon collision with a surface. The partial transfer of energy and momentum is typically modeled by an accommodation coefficient and plays an important role in modeling the forces and heat transfer on spacecraft.

Free molecular flow can be considered collisionless flow because collisions between molecules are so rare that they may be ignored. So a molecule traveling in the freestream flow that impacts the spacecraft surface will bounce off and not come into contact with another molecule as it travels away from the surface. In transitional flow, the intermolecular collisions can no longer be ignored. The collisions are not frequent enough for the flow to be considered continuous, but must be considered to accurately determine the energy and momentum of molecules that reach the surface.

## **5.2 Direct Simulation Monte Carlo**

Direct simulation Monte Carlo (DSMC) is a method developed by Bird<sup>1</sup> to directly model the molecular physics of a gas flow by simulating the flow and collisions of particles. Each particle can represent a large number of real molecules. The velocity and position of the particles are tracked as they move through the simulated physical space. To facilitate the tracking of the particles, the simulated physical region is divided into cells. Ideally, the cell size should be on the same order as the mean free path, but it is acceptable to be larger as long as the flow properties do not change considerably across the cell. The time step used should be less than the mean collision time per particle and also less than the average time for a particle to move across one cell.

The advantage to DSMC is that the movement and collision phases of a particle are decoupled. This means that it is not necessary to track the paths of particles to see if they intersect with other particles and collide. Rather, the collision computations are probabilistic. So the movement is tracked to determine the cell in which a particle resides. Then collision partners are selected using a probability function. The probability of a collision between two molecules in a gas is proportional to the product of the molecules relative velocities and total collision cross section<sup>8</sup>. A random number is assigned to each collision pair. This random number is compared to the collision probability, which is based on kinetic theory of gases. Utilizing the acceptance-rejection method, if the random number is less than the collision probability then the particles will collide, and if the random number is greater than the collision probability the particles will not collide.

Unlike intermolecular collisions, particle collisions with a surface are deterministic. If the particles path crosses any surface, then a collision will occur. When a particle collides with a surface, it transfers some of its momentum to the surface. Then it will be reflected outwards and eventually leave the simulated physical space or collide with another particle or surface. New particles are introduced at boundaries which represent the freestream or other known flow conditions.

Aerodynamic characteristics are calculated from accumulated effects of individual particles colliding with the surface. DSMC will converge to a solution by averaging values over long periods of time after particle interactions reach steady state. Because of computer limitations on the number of particles that can be simulated, some statistical scatter will occur. The statistical scatter in the results is inversely proportional to the square root of the sample size<sup>1</sup>.

In an effort to make DSMC applicable to more complex problems and to ease the requirements on the user, LeBeau<sup>9</sup> developed DSMC Analysis Code (DAC). DAC is able to simulate rarefied gas dynamic environments with complex geometries and flowfield characteristics. One of the benefits of DAC is a special preprocessor. Given the conditions of the flow, such as density and velocity, the preprocessor is able to automatically generate a suitable grid and an appropriate time step for the simulation. The preprocessor uses a two-level embedded Cartesian grid to generate the flowfield cells. After an initial run with a uniform grid, the preprocessor will use these initial results to generate an adapted grid that typically has a higher resolution near the surface (high density regions) and a lower resolution far away from the surface (low density regions). These two levels of resolution allow the results to be more accurate while minimizing the computation time necessary. DAC allows the user to rerun a previous simulation using the previous results as a starting point. The preprocessor can again be used, only now it can use information from the previous simulation to adapt and refine the grid based on the local mean free path of the flow. This adaptation process can be repeated on successive solutions if needed. All DAC simulations performed in this study used one grid adaptation.

DAC also has the ability for parallel implementation, thus greatly reducing the amount of wall-clock time for a simulation. DAC utilizes a flexible boundary scheme that allows the user to input a boundary condition for each element of the surface, such as a solid surface or an out-gassing surface. For this research, the plume is modeled as an out-gassing surface. The plume end cap has a vacuum boundary condition, since in reality gas is not flowing out of the end cap but into the end cap.

DAC has been well verified against other DSMC codes as well as limited flight data and the comparisons have been excellent<sup>9</sup>. DAC has been used for a variety of test cases, two of particular relevance are; shuttle plume loads on a space station and RCS thrusters/freestream interaction. These cases and many more have provided a high level of confidence in the accuracy of DAC.

## Chapter 6. Parametric Study

A parametric study was conducted to determine the sensitivity of the results to changes in the model or parameters used. This study included changing the grid sizes in both the internal nozzle calculations and in the DAC simulations. The source flow model aspect ratio factor and the density multiplier were also varied to determine the sensitivity of the DSMC results to these modeling parameters.

### 6.1. Grid Resolution

For the VNAP CFD calculations of the internal nozzle flow, some of the parametrics have already been discussed, such as changes in smoothing and artificial viscosity. Now changes in the grid resolution will be explored. The original grid resolution used was  $77 \times 18$  in  $x$  and  $y$  respectively. To see if this resolution in the grid was necessary, a coarser grid of  $35 \times 9$  was used. This grid resulted in significant changes in the internal flow. The overall Mach number in the nozzle was reduced, and there was numerical error near the nozzle throat where the Mach number became radically large. It was determined that this grid was too coarse to capture the proper flow.

The next grid used was  $55 \times 14$ . The results of the VNAP calculations with this grid were much closer to the values obtained with the original grid. Although there was still numerical error near the nozzle throat, it was not as severe as with the coarser grid. Since the purpose of calculating the internal nozzle flow is to determine nozzle exit properties to be input into the source flow program, the nozzle exit Mach number profile is compared for each of these three grid resolutions in [Figure 6.1](#). This figure shows that the  $77 \times 18$  grid and the  $55 \times 14$  grid compare well with each other. The two grids only differ by about 3% at the nozzle centerline, and the

boundary layers are nearly identical. The coarser grid of 35×9 shows noticeable differences in the boundary layer and the exit Mach number at the centerline varies by approximately 10% from the value for the 77×18 grid. Another grid with a higher resolution of 100×30 was also used, but the results were almost completely identical with the results of the 77×18 grid. This suggests that further increasing the grid resolution will not yield significant changes to the results and will only serve to increase the computation time. The 77×18 grid is sufficient to accurately capture the results with minimum error introduced due to grid resolution issues.

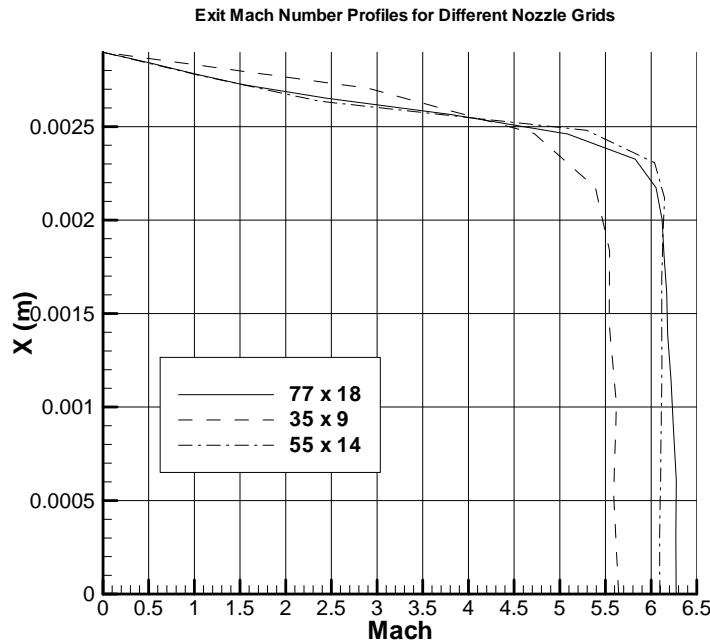


**Figure 6.1.** Nozzle Exit Profile Mach Number for Three Different Grid Resolutions

The grid used for simulated space in the DAC simulations can also be refined. As mentioned previously, the DAC preprocessor automatically generates a suitable grid based on the flow conditions. The preprocessor also has the ability to adapt the grid based on the local mean free path of the previous results for an additional simulation. The refined grid typically requires

longer computation times, but improves the accuracy of the results. All of the simulations were performed using six processors running in parallel. To test sensitivity of the results to the number of grid adaptations performed, an example case is used with two grid adaptations. The example case is for the Odyssey with the RCS-2 thruster active in the nominal aerobraking attitude. The atmospheric density used was  $10 \text{ kg/km}^3$ . It was chosen to have a thruster active since the large gradients surrounding the plume will result in a relatively small local mean free path; thus the grid adaptation will be necessary to refine the grid in the proximity of the plume.

The first DAC simulation performed used a uniform grid of  $38 \times 36 \times 23$ . This uniform grid produces cells that are only slightly greater than the local mean free path near the surface of the spacecraft. The aerodynamic coefficients for the simulation are listed in [Table 6.1](#) in column one. The computation time for the simulations is listed at the bottom of the table in seconds and does not include the time required to run the preprocessor, which is generally small by comparison.

**Table 6.1.** Aerodynamic Coefficients and Computation Time for DAC Simulations of Odyssey with RCS-2 Active for Varying Grids,  $\rho = 10 \text{ kg/km}^3$

	no adaptation	1 adaptation	2 adaptations
Cx	0.1018	0.0790	0.0796
Cy	2.2970	2.2471	2.2479
Cz	0.0425	0.0506	0.0504
Cmx	-0.5059	-0.5037	-0.5034
Cmy	-0.0150	-0.0163	-0.0162
Cmz	0.1023	0.0775	0.0761
time (s)	1032	3224	4253

The second DAC simulation used one grid adaptation based on the results from the uniform grid simulation. The adaptation limited the maximum discretization of any cell to 10 in any direction. The adaptation produced a finer mesh near the plume. The grid was also refined near the back of the solar panel where the plume impingement occurs. In this case, the grid is

generally not refined near the surface of the spacecraft bus or solar panels due to the relatively low-density atmosphere used. Increasing the atmospheric density would result in the grid being refined near the surface upon adaptations. The aerodynamic results of this simulation are listed in column two of [Table 6.1](#). Comparing these results with the results from the previous simulation with no grid adaptation shows some noticeable differences in the aerodynamic coefficients. It is also worth noting that the computation time required to perform the simulation more than tripled with the grid adaptation.

A third DAC simulation was performed using a second grid adaptation based on the results from the first adaptation. This adaptation also limited the discretization of any cell to 10 in any direction. For this simulation, the resultant grid was nearly identical to the previous grid used with only one adaptation. The results were also nearly identical, as can be seen in [Table 6.1](#), although the computation time required did increase significantly. This led to the conclusion that one grid adaptation was sufficient to obtain accurate results. For the remainder of the study, all DAC simulations performed use one grid adaptation.

## 6.2. Source Flow Model

As mentioned in the source flow model section, there are two parameters added to the original model that allow the user to calibrate the model to more detailed solutions, the aspect ratio factor and the density multiplier. The baseline values used for this study are  $AF = 1.6$  and  $DM = 0.4$ . It is desired to determine the sensitivity of the resultant plume flowfield and the results obtained from DAC simulations to changes in these parameters.

Three test cases were performed using various combinations of the two parameters. The first case used  $AF = 1$  and  $DM = 0.4$ . Setting  $AF = 1$  effectively reduces the plume aspect ratio.

An iso-density line for a plume generated using  $AF = 1$  is compared with the same iso-density line from the original plume in [Figure 6.2](#). The number density of each of the lines is  $7.3459e20$ . Comparing the two lines shows that setting  $AF = 1$  results in a much slimmer plume, but the length of the plume remains unchanged. A DAC simulation was then performed using the new plume with RCS-2 active with an atmospheric density of  $10 \text{ kg/km}^3$ . The aerodynamic coefficients resulting are listed in the second column of [Table 6.2](#). Comparing these coefficients with the coefficients obtained from the original plume shows that the coefficients are reduced. A reduction was expected since the plume iso-density surface area is much smaller than the surface area from the previous plume.

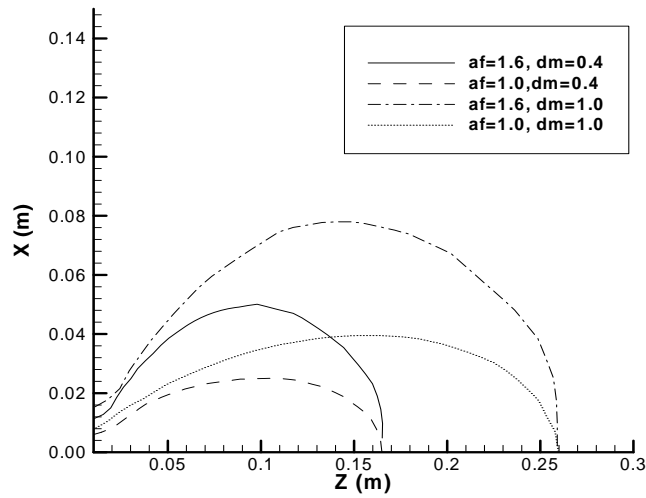


**Figure 6.2.** Plume Iso-density Contours with Varying  $AF$  and  $DM$

**Table 6.2.** Aerodynamic Coefficients from DAC Simulations, Plume Model Varying  $AF$  and  $DM$ , RCS-2 Active,  $\rho = 10 \text{ kg/km}^3$

	$AF = 1.6$ $DM = 0.4$	$AF = 1$ $DM = 0.4$	$AF = 1.6$ $DM = 1$	$AF = 1$ $DM = 1$
$F_x$	0.1008	0.0524	0.1930	0.1192
$F_y$	2.8675	2.7057	3.2194	2.8529
$F_x$	0.0646	0.0104	0.1441	0.0429
$M_x$	-3.0468	-2.9333	-3.2970	-3.0356
$M_y$	-0.0986	-0.0322	-0.1965	-0.0668
$M_z$	0.4689	0.1828	1.1383	0.4818
$C_x$	0.0790	0.0410	0.1512	0.0934
$C_y$	2.2471	2.1203	2.5229	2.2357
$C_z$	0.0506	0.0082	0.1129	0.0336
$C_{m_x}$	-0.5037	-0.4850	-0.5451	-0.5019
$C_{m_y}$	-0.0163	-0.0053	-0.0325	-0.0110
$C_{m_z}$	0.0775	0.0302	0.1882	0.0797

The second test case kept the aspect ratio factor at its original value of 1.6 and increased the density multiplier to 1. Again, setting the density multiplier to 1 effectively increases the density uniformly over the baseline case. The resultant iso-density line is compared with the other cases in [Figure 6.2](#). As expected, increasing the density multiplier resulted in a larger iso-density surface, which retains the same shape as the original plume because the attenuation was not altered. The results of the DAC simulation with the new plume are shown in the third column of [Table 6.2](#). The coefficient magnitudes are larger than the coefficients from the previous cases due to the increased size of the plume iso-density surface.

The third test case altered both the aspect ratio factor to 1 and the density multiplier to 1. With both of these values set equal to one, the modified source flow code should return a flowfield identical to the flowfield produced by the source flow code before modification. The iso-density line for this simulation is shown in [Figure 6.2](#), along with the previous iso-density lines. The line displays the expected characteristics, elongated because of the increased density multiplier and slim due to the reduced aspect ratio factor. The results from the DAC simulation

with this plume are shown in the fourth column of [Table 6.2](#). It is interesting to note that, although the shape of the plumes are very different, the coefficients obtained from the simulation with this plume are close to the coefficients obtained from the simulation with the original plume using  $AF = 1.6$  and  $DM = 0.4$ .

# Chapter 7. Application to Mars Odyssey

## 7.1 Baseline Aerodynamics

DSMC simulations were initially performed with the spacecraft at nominal attitude (zero pitch and yaw) with respect to the freestream velocity for varying densities to provide a baseline set of forces and moments with no RCS plumes present. The density values were chosen to anticipate the range of densities the spacecraft would experience during aerobraking. MGS experienced a range of densities from  $2.09 \text{ kg/km}^3$  to  $80.9 \text{ kg/km}^3$  although the majority of aerobraking took place at the lower densities because of limitations imposed by a broken latch on one of the solar panels. Odyssey was expected to experience densities up to or greater than  $100 \text{ kg/km}^3$ . With this reasoning, the densities chosen were; 1, 3, 10, 32 and  $100 \text{ kg/km}^3$ . These densities form evenly spaced intervals on a log base ten plot. DAC provides aerodynamic results as forces and moments about the origin. The forces and moments were converted to coefficient form where appropriate based on a spacecraft reference area of  $11.03 \text{ m}^2$  and a reference length of 4.74 m. The moments were shifted to be about the spacecraft center of mass during the midpoint of aerobraking. The center of mass used was;  $x = -0.0629$ ,  $y = -0.0172$ , and  $z = 1.11$ . The results of these simulations are included in [Table 7.1](#).

One of the first things that can be observed from [Table 7.1](#) is that the spacecraft in the nominal attitude is not trimmed. This is evident by the fact that there are nonzero aerodynamic moments on the spacecraft. It can also be seen that the force and moment coefficients on the spacecraft generally decrease with increasing density, which is expected. The coefficient of force in the Y-direction is much larger than the other coefficients because the freestream velocity is in

the Y-direction, so the drag is predominately in the Y-direction. The surface pressure contours on the Odyssey with a free stream density of  $100 \text{ kg/km}^3$  are shown in **Figure 7.1**. The results from these DSMC simulations will serve as comparisons for later simulations with the plumes added.

**Table 7.1.** Aerodynamic Coefficients for Mars Odyssey with Varying Densities (Moments are about CM)

	1 kg/km <sup>3</sup>	3 kg/km <sup>3</sup>	10 kg/km <sup>3</sup>	32 kg/km <sup>3</sup>	100 kg/km <sup>3</sup>
Qinf	0.0116	0.0366	0.1157	0.3659	1.1569
Cx	-0.0002	0.0001	0.0005	0.0021	0.0059
Cy	2.1322	2.1046	2.0588	2.0203	1.9457
Cz	-0.0041	-0.0061	-0.0106	-0.0182	-0.0286
Cmx	0.0048	0.0047	0.0044	0.0043	0.0043
Cmy	-0.0005	-0.0008	-0.0013	-0.0012	-0.0014
Cmz	0.0301	0.0300	0.0284	0.0277	0.0255

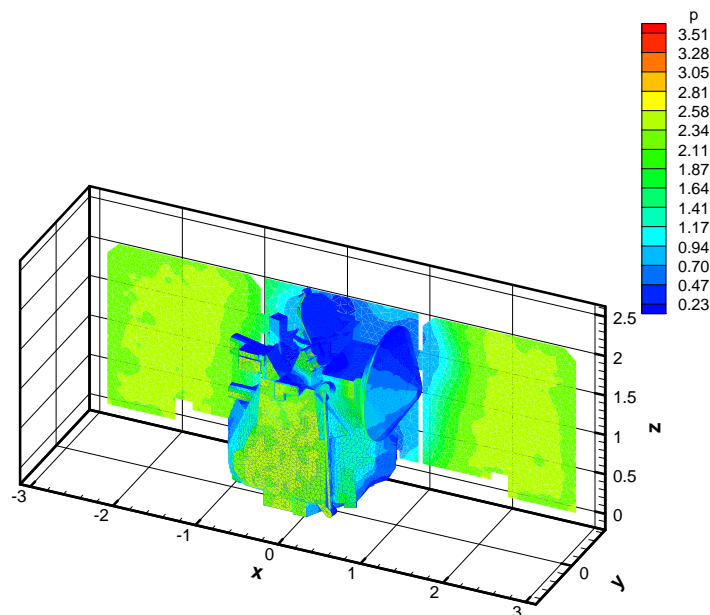


**Figure 7.1.** Odyssey Surface Pressure Contour, No Plumes,  $\rho_\infty=100 \text{ kg/km}^3$

## 7.2 RCS Study

With the reference cases completed, cases with RCS thruster firings were performed. The RCS thrusters for Odyssey may be fired individually or in combinations of two thrusters. However, it was decided to consider just one plume initially, so that the influence of the plume impingement and flowfield interaction effects could be determined without having to consider possible plume-plume interaction effects. Based on the symmetry of the spacecraft and the RCS thruster arrangement, two cases were chosen, one with the RCS-1 thruster firing and one with the RCS-2 thruster firing. To obtain the maximum possible plume-flowfield interaction effects, these cases were run at the atmospheric density of  $100 \text{ kg/km}^3$ . The results of these DSMC simulations are shown in [Table 7.2](#).

**Table 7.2.** Aerodynamic Coefficients about CM for Mars Odyssey With Plumes, Density =  $100 \text{ kg/km}^3$

	s/c	s/c & RCS-1	s/c & RCS-2
Cx	0.0059	0.0054	0.0070
Cy	1.9457	1.9161	1.9577
Cz	-0.0286	-0.0163	-0.0199
Cmx	0.0043	0.0017	0.0044
Cmy	-0.0014	-0.0093	-0.0071
Cmz	0.0255	0.0160	0.0326

The coefficients of moment are about the spacecraft center of mass. These results represent only aerodynamic and impingement forces and do not include the thrust from the firing. The aerodynamic coefficients from the previous simulations with no plumes at the same atmospheric density are included in the table for comparison. It can be seen that both RCS-1 and RCS-2 plumes have a small but observable impact on the coefficients of forces and moments on

the spacecraft. The surface pressure contours with RCS-1 firing and RCS-2 firing are shown in **Figures 7.2** and **7.3** respectively. The direct impingement

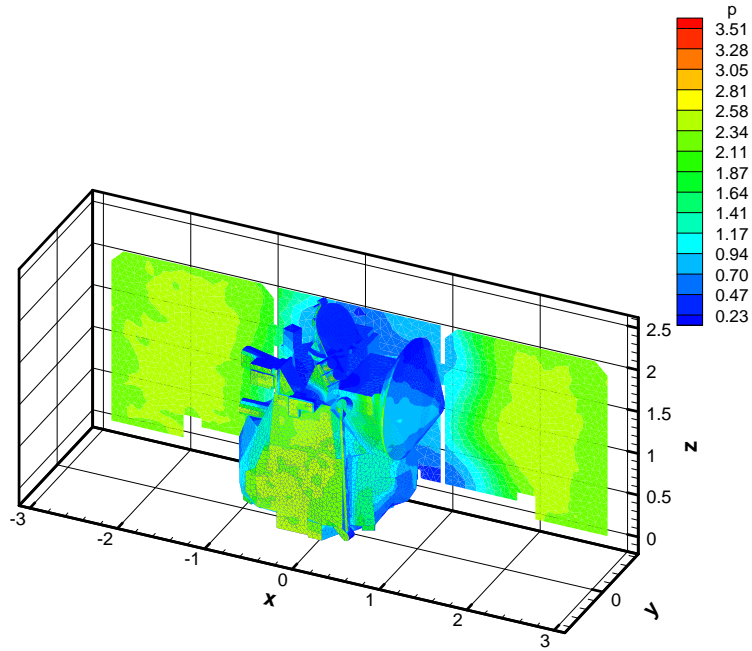


**Figure 7.2.** Odyssey Surface Pressure Contour, RCS-1 Plume,  $\rho_{\infty}=100 \text{ kg/km}^3$

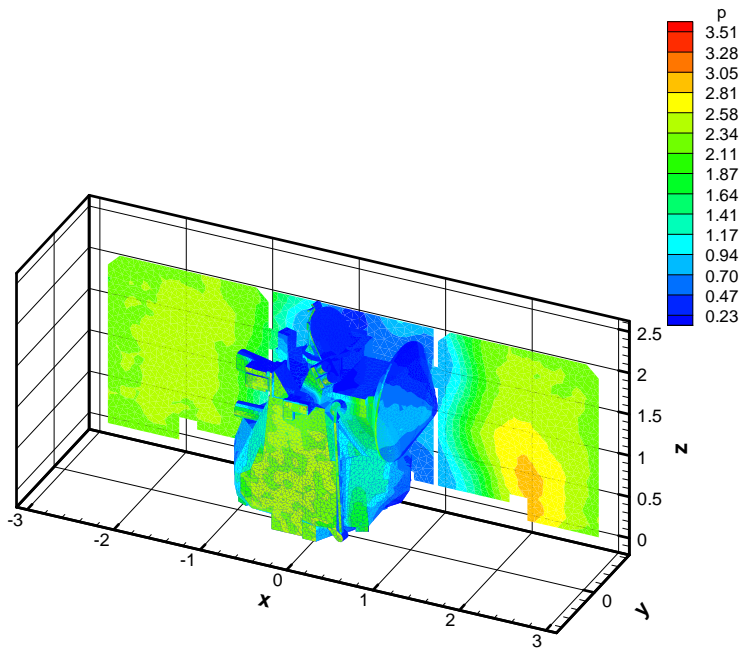


**Figure 7.3.** Odyssey Surface Pressure Contour, RCS-2 Plume,  $\rho_{\infty}=100 \text{ kg/km}^3$

of the plume onto the solar panel is evident for RCS-2. This direct impingement occurs because the RCS-2 nozzle is canted toward the panel.

It is now important to determine how these moment coefficients compare to those caused by the thrust. The forces are not included in this comparison since the attitude is the primary concern for this study. **Table 7.3** shows the moments caused by aerodynamics only (including plume-flowfield interactions), moments caused by thrust only, and the combination of the two.

**Table 7.3.** Breakdown of RCS Thrust and Aerodynamic Forces,  
Density = 100 kg/km<sup>3</sup>

Moment Coefficients about CM, aerodynamic forces only

	s/c	s/c & RCS-1	s/c & RCS-2
Cmx	0.0043	0.0017	0.0044
Cmy	-0.0014	-0.0093	-0.0071
Cmz	0.0255	0.0160	0.0326

Moment Coefficients about CM, thrust forces only

	s/c	s/c & RCS-1	s/c & RCS-2
Cmx	0.0000	0.0037	-0.0037
Cmy	0.0000	0.0132	0.0132
Cmz	0.0000	0.0128	-0.0123

Moment Coefficients about CM, thrust and aerodynamic forces

	s/c	s/c & RCS-1	s/c & RCS-2
Cmx	0.0043	0.0053	0.0007
Cmy	-0.0014	0.0039	0.0062
Cmz	0.0255	0.0288	0.0203

From [Table 7.3](#), it can be seen that the plume impingement and aerodynamic moments are smaller than the thrust moments, but are of a comparable magnitude. Since the plumes induce moments that sometimes oppose the thrust moments, it is important that RCS effects be considered in any 6-DOF simulations of the spacecraft attitude and attitude rates with RCS firings.

RCS interactions during aerobraking are composed of two components, impingement and flowfield interaction. It is possible to look at the effect of each of these components separately. To do this the same cases can be analyzed with a zero density atmosphere. With no atmosphere, all of the non-thrust forces and moments on the spacecraft will be a result of plume impingement only. With the assumption that the plume impingement forces do not change with the addition of an atmosphere, then the plume-flowfield interaction forces and moments can be calculated as the difference between the forces and moments caused by the RCS firing with and without an atmosphere. The assumption that the impingement forces do not change is probably a reasonable assumption in these cases since the spacecraft is still in the low-density rarefied flow regime for all densities of interest. The breakdown between moments caused by plume impingement and plume-flowfield interaction for RCS-2 is shown in [Table 7.4](#). The table also includes the coefficients of moment caused by thrust to serve as a comparison of magnitudes. The plume impingement moments are larger in magnitude than the plume-flowfield interaction moments but in opposite directions for the x and z components. It should be noted that the combined moments caused by the RCS-2 firing all are in the opposite direction of the thrust. The thrust has the larger magnitude, but because of the RCS-2 aerodynamic effects the thruster's effectiveness is reduced.

**Table 7.4.** RCS-2 Plume Impingement and Flowfield Interaction Effects  
about CM, Density = 100 km/kg<sup>3</sup>

	A	B	C	D	E	F
Mx	0.26057	0.26591	0.00534	0.19790	-0.19256	-0.22860
My	-0.08261	-0.42892	-0.34631	-0.19401	-0.15230	0.80130
Mz	1.54430	1.97221	0.42791	0.60926	-0.18135	-0.74630
Cmx	0.0043	0.0044	0.0001	0.0033	-0.0032	-0.0037
Cmy	-0.0014	-0.0071	-0.0057	-0.0032	-0.0025	0.0132
Cmz	0.0255	0.0326	0.0071	0.0101	-0.0030	-0.0123

A = Aerodynamic moments on Odyssey, no RCS

B = Aerodynamic moments on Odyssey, with RCS-2

C = Total RCS-2 interaction (B-A)

D = RCS-2 impingement

E = RCS-2 flowfield interaction (C-D)

F = RCS-2 thrust only

### 7.3 RCS Database Construction

A Program to Optimize Simulated Trajectories (POST) was used for 6-DOF simulations of Odyssey. POST can be used for vehicle modeling, trajectory simulation, and targeting and optimization. Aerodynamic and atmospheric models can be implemented to simulate the rotational motion of the spacecraft throughout aerobraking. POST has been used successfully to solve a wide variety of atmospheric ascent and reentry problems along with analysis of many planetary exploration missions<sup>10</sup>.

To incorporate the RCS plume effects into a POST 6-DOF simulation of Odyssey during aerobraking, a database was constructed to account for all possible RCS firings over the full range of aerobraking densities and spacecraft attitudes. A database had already been constructed for the POST 6-DOF simulations to provide the aerodynamic coefficients for the Odyssey as a function of attitude and density in the absence of RCS firings. The RCS database compliments the original database to include the change in aerodynamic coefficients as a result of the RCS firings.

A computer subroutine was developed that incorporates the RCS aerodynamic effects for POST simulations. The subroutine requires the attitude, density and thruster on/off as input. The database is then called to determine the change in aerodynamic coefficients. Linear interpolation is used to interpolate coefficients between angles and density. To simplify the programming, the database is actually split up into four separate databases, one for each RCS thruster.

Construction of the database required additional DSMC simulations to capture the variation in plume-flowfield interactions with density and attitude to an acceptable accuracy. Depending on the atmospheric density used, a single case run in DAC using six processors in parallel can take up to a day to complete. Assuming the flight corridor to be +/- 15° in both pitch and yaw, it would be ideal to perform DSMC simulations for combinations of pitch and yaw over a +/- 20° corridor using 5° increments. A larger range of angles than the specified corridor limits should be used since the corridor limits only specify when the RCS thrusters are activated. The 5° increments would match the increments used in the aerodynamic database without RCS firings. A matrix containing these combinations would require eighty-one simulations to complete. Factoring in that this matrix is desired for five different densities and four different RCS thrusters and the total amount of simulations needed would be 1620. This value does not even include running DAC simulations with multiple thruster firings.

At roughly one day per simulation, it is obviously not feasible to perform all of these simulations in DAC. To complete the database in the timeframe needed, some simplifying assumptions were made. The first major assumption was that superposition can be used to account for multiple simultaneous firings. To test this assumption, three situations were looked

at, superposition with RCS-2 and RCS-3, with RCS-1 and RCS-3, and with RCS-1 and RCS-2.

Refer to [Table 7.5](#) for the results (in dimensional form).

**Table 7.5.** Superposition of RCS Effects for Multiple Thruster Firings about the CM, Density = 100 km/kg<sup>3</sup>

RSC-2 & RCS-3

	(1) s/c alone	(2) s/c & RCS-2	(3) s/c & RCS-3	(4) = (2) - (1) RCS-2 alone	(5) = (3) - (1) RCS-3 alone	(6) Thrust alone	(6) = (1) + (4) + (5) Superposition	(7) s/c & RCS-2 & RCS-3	(8) = (7) - (6) Error
Fx	0.0751	0.0892	0.0158	0.0141	-0.0593	0.0000	0.0299	0.0597	0.0299
Fy	24.8291	24.9823	25.0012	0.1532	0.1721	-0.7406	25.1543	25.1143	-0.0400
Fz	-0.3652	-0.2541	-0.2653	0.1111	0.0999	-0.3088	-0.1542	-0.1597	-0.0055
Mx	0.2606	0.2659	0.2445	0.0053	-0.0160	-0.4571	0.2499	0.2787	0.0288
My	-0.0826	-0.4289	0.2192	-0.3463	0.3019	0.0194	-0.1271	-0.1265	0.0006
Mz	1.5443	1.9722	1.1573	0.4279	-0.3870	-0.0466	1.5852	1.5048	-0.0804
Cmx	0.0043	0.0044	0.0040	0.0001	-0.0003		0.0041	0.0046	0.0005
Cmy	-0.0014	-0.0071	0.0036	-0.0057	0.0050		-0.0021	-0.0021	0.0000
Cmz	0.0255	0.0326	0.0191	0.0071	-0.0064		0.0262	0.0249	-0.0013

RSC-1 & RCS-3

	(1) s/c alone	(2) s/c & RCS-1	(3) s/c & RCS-3	(4) = (2) - (1) RCS-1 alone	(5) = (3) - (1) RCS-3 alone	(6) Thrust	(6) = (1) + (4) + (5) Superposition	(7) s/c & RCS-1 & RCS-3	(8) = (7) - (6) Error
Fx	0.0751	0.0069	0.0158	-0.0682	-0.0593	0.0000	-0.0524	-0.0269	0.0255
Fy	24.8291	24.4513	25.0012	-0.3778	0.1721	0.0000	24.6234	24.6384	0.0151
Fz	-0.3652	-0.2077	-0.2653	0.1575	0.0999	-0.3088	-0.1078	-0.0880	0.0197
Mx	0.2606	0.1002	0.2445	-0.1603	-0.0160	-0.0053	0.0842	0.1104	0.0262
My	-0.0826	-0.4939	0.2192	-0.4113	0.3019	0.0194	-0.1921	-0.2273	-0.0353
Mz	1.5443	0.9685	1.1573	-0.5758	-0.3870	1.4734	0.5816	0.5757	-0.0059
Cmx	0.0043	0.0017	0.0040	-0.0027	-0.0003		0.0014	0.0018	0.0004
Cmy	-0.0014	-0.0082	0.0036	-0.0068	0.0050		-0.0032	-0.0038	-0.0006
Cmz	0.0255	0.0160	0.0191	-0.0095	-0.0064		0.0096	0.0095	-0.0001

RSC-1 & RCS-2

	(1) s/c alone	(2) s/c & RCS-1	(3) s/c & RCS-2	(4) = (2) - (1) RCS-1 alone	(5) = (3) - (1) RCS-2 alone	(6) Thrust	(6) = (1) + (4) + (5) Superposititon	(7) s/c & RCS-1 & RCS-2	(8) = (7) - (6) Error
Fx	0.0751	0.0069	0.0892	-0.0682	0.0141	-1.5882	0.0210	0.0004	-0.0206
Fy	24.8291	24.4513	24.9823	-0.3778	0.1532	0.0000	24.6045	24.7217	0.1172
Fz	-0.3652	-0.2077	-0.2541	0.1575	0.1111	-0.3088	-0.0966	-0.1329	-0.0364
Mx	0.2606	0.1002	0.2659	-0.1603	0.0053	-0.0053	0.1056	0.0660	-0.0396
My	-0.0826	-0.4939	-0.4289	-0.4113	-0.3463	1.6026	-0.8402	-0.6931	0.1472
Mz	1.5443	0.9685	1.9722	-0.5758	0.4279	0.0273	1.3965	1.5190	0.1225

For example purposes, the focus will be on the superposition using RCS-2 and RCS-3. At nominal attitude and a density of  $100 \text{ kg/km}^3$ , four simulations were performed. The first simulation was with no plumes. Then two simulations were performed, one with only RCS-2 firing and another with only RCS-3 firing. With these three simulations, the change in coefficients caused by RCS-2 and RCS-3 were determined separately. Based on the assumption of superposition, a simulation with both RCS-2 and RCS-3 firings should give the same change in coefficients as just adding the two separate change in coefficients. The two separate sets of delta coefficients for individual thruster firings were added and compared to the delta coefficients obtained from a DAC simulation with both RCS-2 and RCS-3 firing simultaneously. The difference between the actual values and the superposition approximation values are shown in column 8 of [Table 7.5](#). The superposition assumption for this case appears to be a reasonably good assumption, with errors less than 10% of the total moment. It is also shown to be a good assumption for the other two cases as well. Superposition eliminates the need to perform DSMC simulations for combinations of thruster firings including thruster firings that result in plume-plume interactions.

The next major assumption is that the change in coefficients caused by RCS-3 and RCS-4 firings can be determined from the change in coefficients caused by RCS-2 and RCS-1 firings respectively. This assumption is made possible by the symmetry of the spacecraft. The relationships used between RCS-2 and RCS-3 coefficients and RCS-1 and RCS-4 coefficients are shown in [Table 7.6](#). With this assumption, the simulations required are cut in half since no runs will be performed for RCS-3 and RCS-4.

**Table 7.6.** Conversion from RCS-1 and RCS-2 to RCS-4 and RCS-3

RCS-1	RCS-4	RCS-2	RCS-3
Del Cx =	- Del Cx	Del Cx =	- Del Cx
Del Cy =	Del Cy	Del Cy =	Del Cy
Del Cz =	Del Cz	Del Cz =	Del Cz
Del Cmx =	Del Cmx	Del Cmx =	Del Cmx
Del Cmy =	- Del Cmy	Del Cmy =	- Del Cmy
Del Cmz =	- Del Cmz	Del Cmz =	- Del Cmz

To begin building the database, pitch and yaw combinations of three angles (-15°, 0°, 15°) were used. This reduces the number of combinations at each density from eighty-one to nine. To further reduce the number of simulations, an interpolation scheme was developed to interpolate values between densities. First, the nominal attitude case was performed at each density twice, once with RCS-1 firing and once with RCS-2 firing. With the data from these simulations, plots were obtained that show how the coefficients vary with density. These plots are shown in [Figures 7.4 – 7.7](#). It is assumed that the coefficients for different attitudes will vary in a similar manner. To get the coefficients at the endpoints for each attitude, the 3x3 attitude matrix was completed for densities of 1 and 100 kg/km<sup>3</sup>. Then, using the functional variation with density for the nominal attitude, the database was filled in for the three densities between 1 and 100 kg/km<sup>3</sup> at other attitudes.

With a coarse database complete for each of the thrusters, the database was enhanced utilizing a curve fitting technique. First, for each pitch angle, a second order polynomial curve was used to fit the data for each delta coefficient vs. yaw angle. This polynomial curve was used to enrich the database into five-degree increments with respect to yaw. Then the same process was performed for each yaw angle, and a second order polynomial curve was used to fit the data

for each delta coefficient vs. pitch angle. When this step was completed, the database was fully populated from  $-20^\circ$  to  $20^\circ$  in both

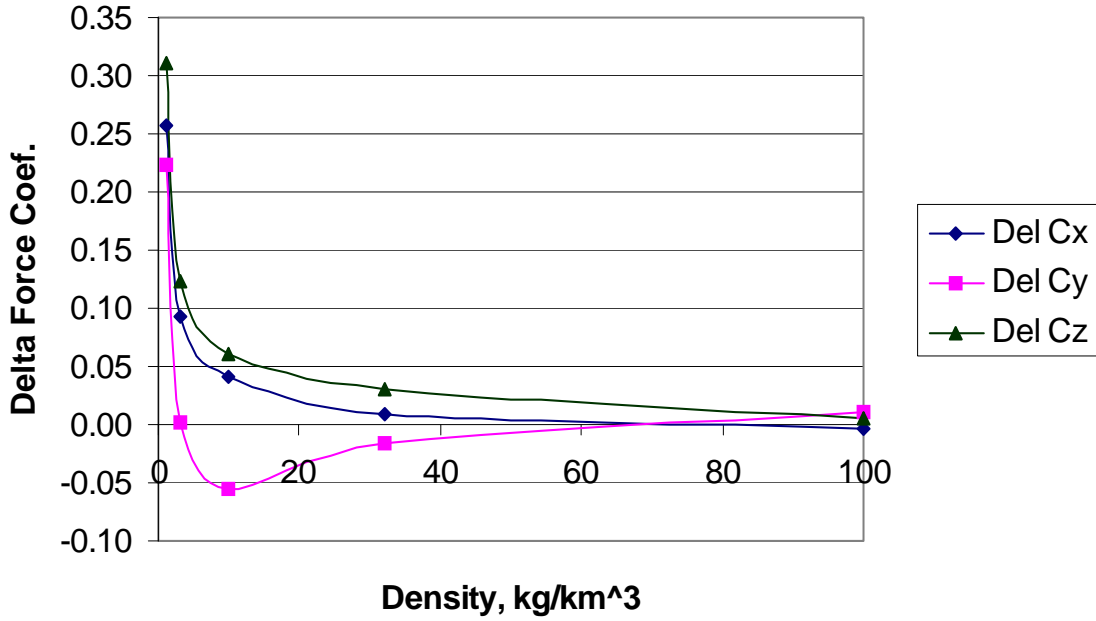


Figure 7.4. Delta Force Coefficients vs. Density, RCS-1, Nominal

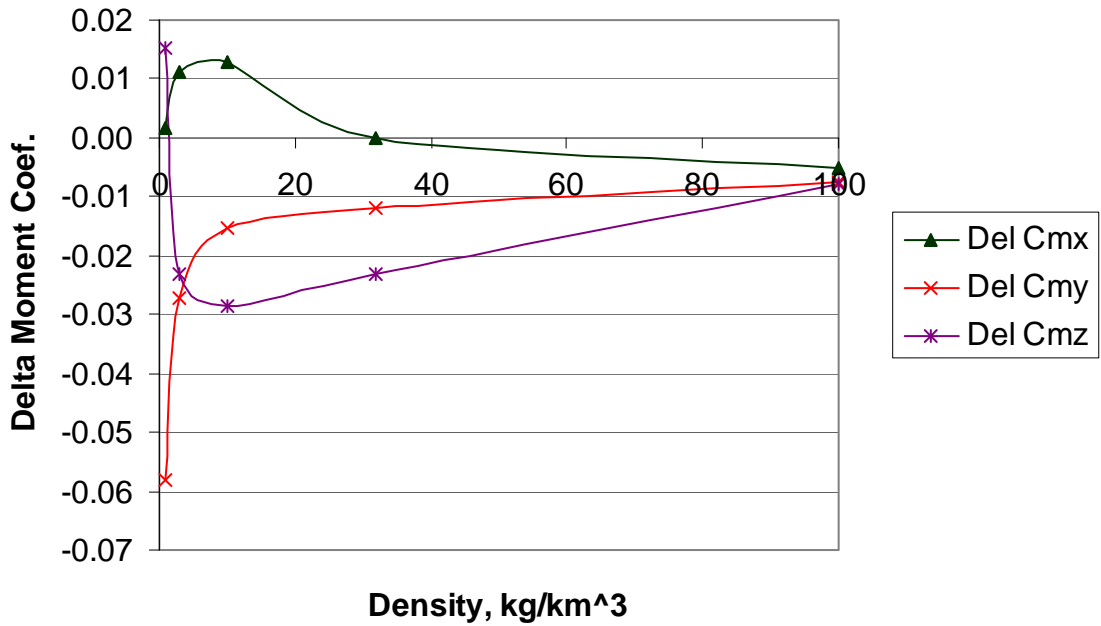


Figure 7.5. Delta Moment Coefficients vs. Density, RCS-1, Nominal

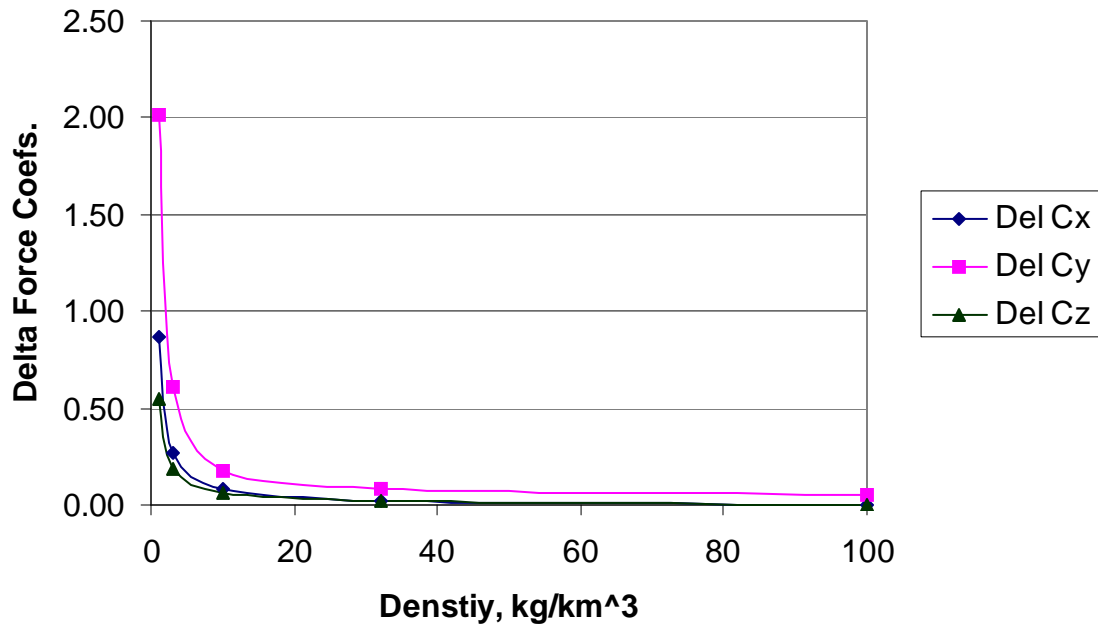


Figure 7.6. Delta Force Coefficients vs. Density, RCS-2, Nominal

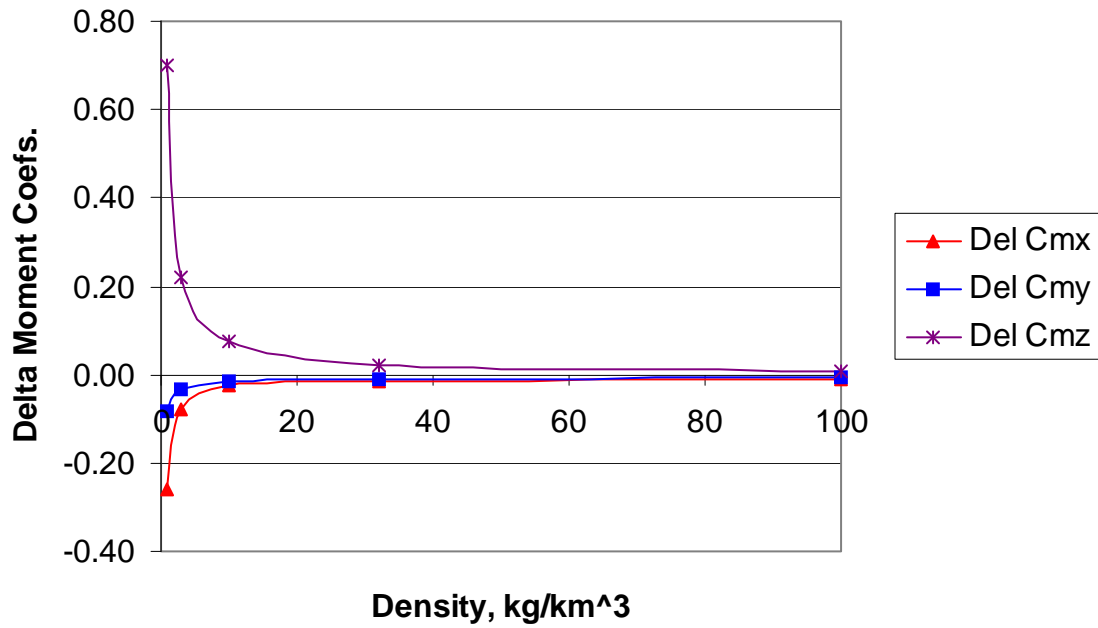


Figure 7.7. Delta Moment Coefficients vs. Density, RCS-2, Nominal

pitch and yaw in five-degree increments for both densities of 1 and 100 kg/km<sup>3</sup>. The coefficients for the varying attitudes at the densities in between were interpolated using the previously described procedure for interpolating between densities.

A separate subroutine was developed to incorporate the actual thrust force caused by the thruster firings into the POST 6-DOF simulations. This was separated from the RCS plume subroutine so that each subroutine could be turned on and off individually to study the effects on the aerodynamics. The subroutine takes the thruster on/off as input. A constant thrust of 0.8896 N is applied at the nozzle throat of the firing thrusters. The moments are taken about the spacecraft origin and then the subroutine gives POST the forces and moments for the thrusters in dimensional form.

#### **7.4 Effects on the Aerodynamics**

With the database complete, it is useful to observe general trends for the change in aerodynamic coefficients caused by the thruster firings with varying attitude and density. The previous [Figures 7.4 – 7.7](#) show that the changes in force and moment coefficients tend to decrease in magnitude as the density is increased. This is expected since the coefficients are normalized by the freestream dynamic pressure, which increases as the atmospheric density increases. That is also why the changes in the coefficients become asymptotic as they approach large density.

The plumes from RCS-1 and RCS-4 have more of an effect on the aerodynamics than the plumes from RCS-2 and RCS-3. This can be explained physically by the thruster locations. RCS-1 and RCS-4 are both located near the backside of the solar panels and are pointed away from the panels. The plumes from these thrusters interact with the flowfield and create a

shadowing effect, where the pressure is reduced on a portion of the solar panel. The reduced pressure on the solar panel reduces the aerodynamic forces and moments on the panel. The plumes created by firing the RCS-2 and RCS-3 thrusters also have a similar shadowing effect caused by the plumes interacting with the flowfield, but since both of these thrusters are pointing towards the backside of the solar panels they also impinge on the panels. The forces and moments caused by the impingement tend to largely cancel out the forces and moments caused by the plume-flowfield interaction. This can be observed in [Table 7.4](#).

It should also be noted that plume impingement causes shear forces on the panel in the x and z directions due to skin friction. Shear forces in the x direction are the larger of the two components but have a smaller moment arm than forces in the z direction about the center of mass. Shear forces in x will produce a yawing moment while shear forces in z will produce a rolling moment. Therefore, the resultant effects of RCS firings are a complex combination of pressure and shear forces resulting from both impingement and flow interactions.

## Chapter 8. Validation of Application to Odyssey

To provide confidence that the RCS plume effects are being correctly incorporated into the POST 6-DOF simulations, both the developed subroutine and the database need to be validated.

### 8.1 POST Simulation Results

A test program was developed to assure that the subroutine returned the intended values from the database. The test program provided multiple inputs to the subroutine for which the results had been determined independently. The inputs tested the ability of the program to perform a table lookup, add effects from multiple thruster firings, interpolate in pitch, interpolate in yaw, interpolate in density, and to display warning labels for extrapolated data. For all of these cases the subroutine returned the proper values. This implies that the subroutine and its internal interpolating schemes are working properly. The thrust subroutine was also tested in a similar manner and gave the expected results.

Interpolation schemes were used to enrich the database from a minimal amount of DSMC simulations and then the POST subroutine further interpolates the results based on the database values. It is necessary to ensure that the changes in aerodynamic coefficients caused by the thruster firings are not lost in the interpolation error. This was achieved by first selecting random attitudes and densities, and then performing DSMC simulations with and without a thruster firing. Four cases were studied. A case (RCS-2 active, pitch =  $10^\circ$ , yaw =  $0^\circ$ , density =  $10 \text{ kg/km}^3$ ) with typical results was chosen for example purposes. The results for this case are shown in [Table 8.1](#). The first column lists the results for the DSMC simulation with no thrusters active, and the second

column shows the results with RCS-2 active. Next, the changes in coefficients are determined and are compared to the database predicted changes in coefficients. The interpolation error is defined as the difference between the delta coefficients as determined by the DSMC simulations and the predicted delta coefficients from the interpolated database. Comparing the interpolation errors to the actual delta coefficients shows that the delta coefficients are significantly larger than the interpolation errors. This leads to the conclusion that the delta coefficients are significant for the simulation and are not lost in the interpolation error.

**Table 8.1.** Comparing Delta Coefficients to Interpolation Error, RCS-2 Active, Pitch = 10°, Yaw = 0°,  $\rho = 10\text{kg/km}^3$

	s/c alone	s/c & RCS-2	RCS-2 alone	predicted effect	interpolation error
Cx	0.0008	0.0730	0.0722	0.0730	-0.0008
Cy	2.0275	2.2427	0.2152	0.1908	0.0244
Cz	-0.3206	-0.2446	0.0760	0.1027	-0.0267
Cmx	-0.5051	-0.5315	-0.0264	-0.0189	-0.0075
Cmy	-0.0002	-0.0231	-0.0229	-0.0182	-0.0047
Cmz	0.0027	0.0820	0.0794	0.0778	0.0016

## 8.2 Odyssey Flight Data Comparison

Once Odyssey began aerobraking in late October, it started sending back flight data. POST simulations were compared to the flight data to determine the accuracy of the simulations. For the early orbits, the spacecraft did not dip far into the atmosphere so the densities were low. The subroutine to include the RCS plume effects was not intended to be used at very low densities, so it was inactive. The thrust subroutine was activated for the simulations though. A comparison of the attitude rates for an early aerobraking pass and the POST simulation is shown in [Figure 8.1](#). From this figure it can be observed that the thruster firing effects are the most

noticeable on the roll rate. The pitch rate and the yaw rate remain relatively smooth during the series of thruster firings from about 70 seconds to 200 seconds after periapsis. The POST simulation matches up

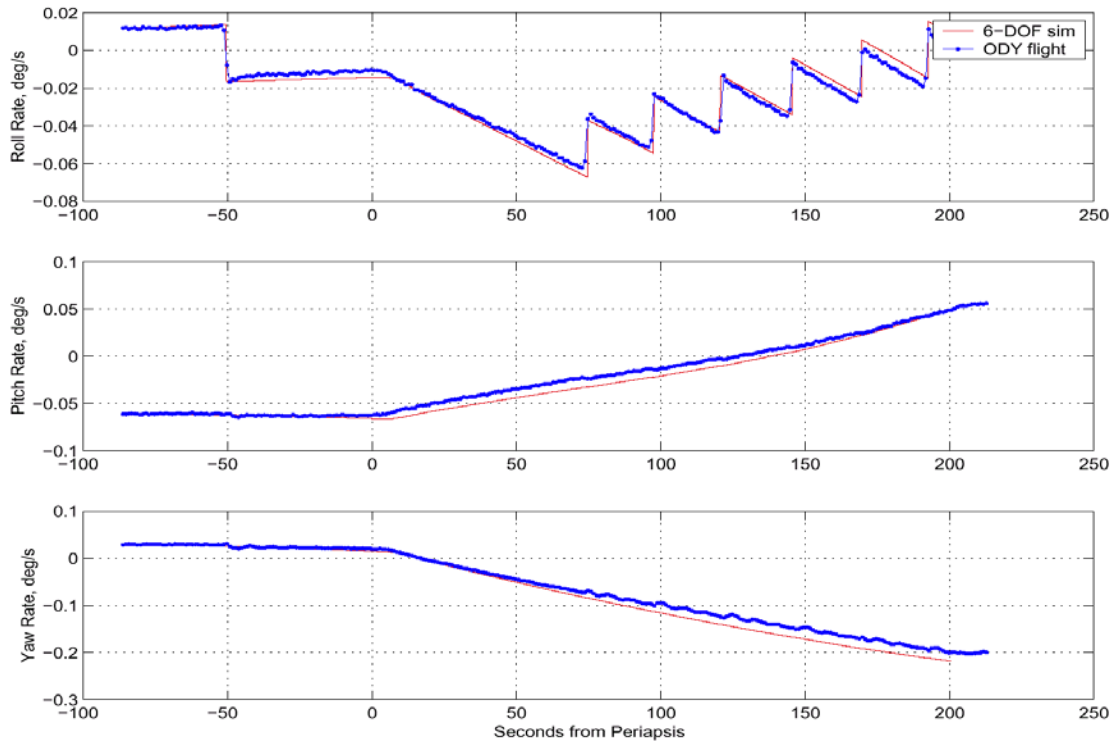


**Figure 8.1.** Attitude Rates Comparison of POST 6-DOF Simulation to Flight Data, Orbit 6, RCS Model Inactive, Thrust Model Active

very well with the flight data, especially for the thruster firings in the roll rate. The next two figures, [Figures 8.2](#) and [8.3](#), show comparisons of the attitude and the aero angles for the same orbit. The simulation still matches up well with the flight data, but it is noticeable that the results begin to diverge as time after periapsis increases. This is mainly due to the fact that the error in the simulation is accumulative, and as the time proceeds the error will steadily grow. These results lead to the conclusion that the overall POST simulation is working and the thruster subroutine is also working properly.

Now a POST simulation is compared to flight data for typical densities experienced during an aerobraking pass. Orbit 24 was chosen to represent a typical pass. Two simulations were performed for this orbit, one with the RCS plume effects.

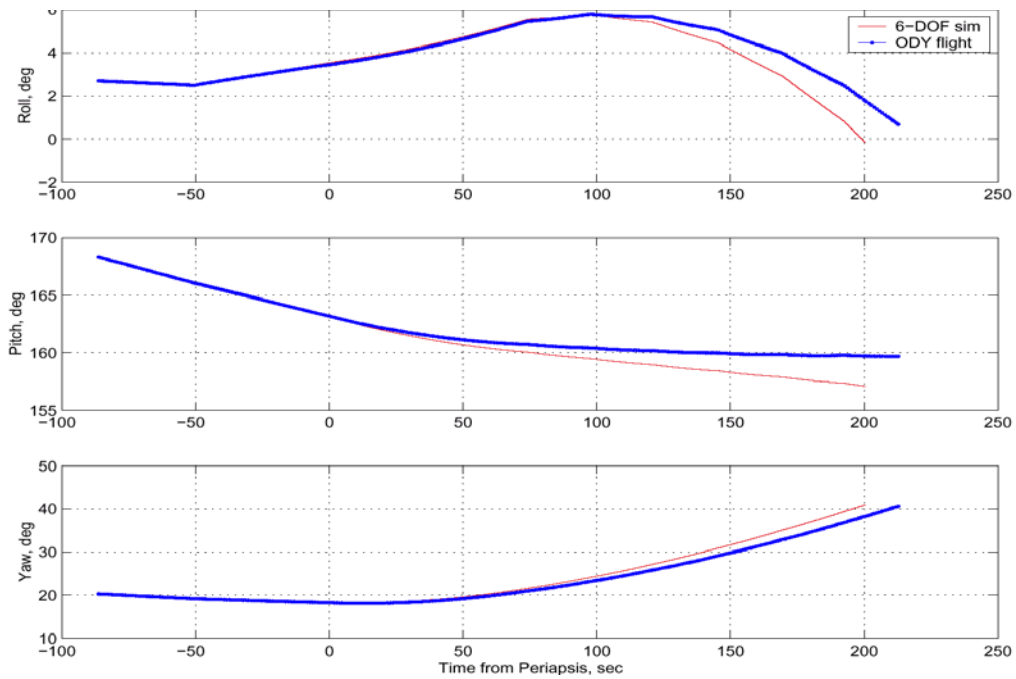


**Figure 8.2.** Attitude Comparison of POST 6-DOF Simulation to Flight Data, Orbit 6, RCS Model Inactive, Thrust Model Active

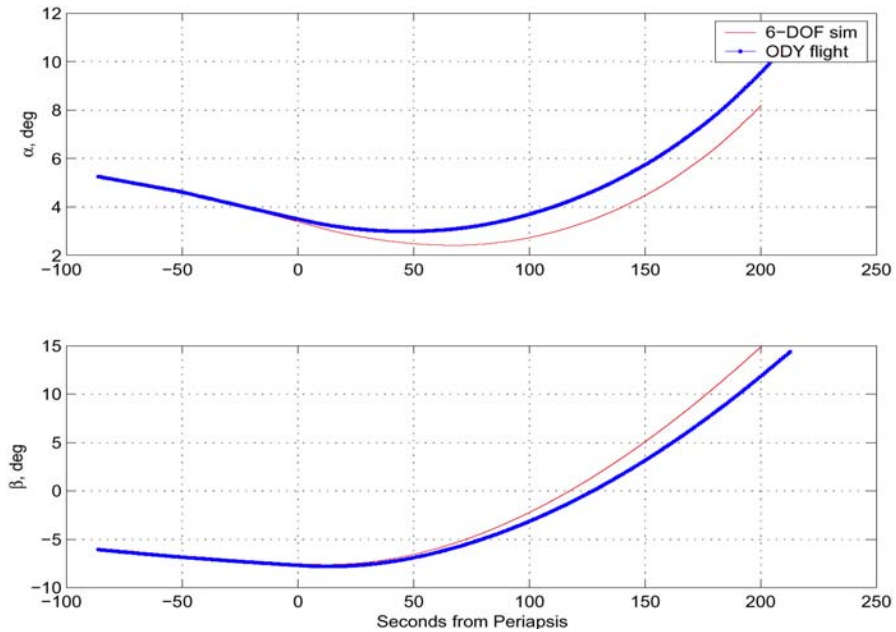


**Figure 8.3.** Aero Angles Comparison of POST 6-DOF Simulation to Flight Data, Orbit 6, RCS Model Inactive, Thrust Model Active

subroutine active and one with it inactive. The attitude rates for this pass are shown in [Figure 8.4](#). For the roll rate, there are significant differences between the simulation and flight data and including the RCS plume effects subroutine improves the predictions by about a factor of two. For the pitch rate and the yaw rate, there is more reasonable agreement between the simulation and flight data and RCS firings have little effect until the end of the pass. The aero angles for this pass are shown in [Figure 8.5](#). Again, inclusion of the RCS plume effects subroutine has very little effect on the angles. The attitude for the pass is shown in [Figure 8.6](#). Here, there is a noticeable effect on the simulation results by the inclusion of the RCS plume effects model. The model greatly improves the predictions after periapsis in roll, pitch, and yaw. Overall the RCS model allows the POST 6-DOF simulations to match more closely with the actual Odyssey flight data.

Orbit 24 represents the typical aerobraking pass and a similar conclusion can be drawn for most other passes.

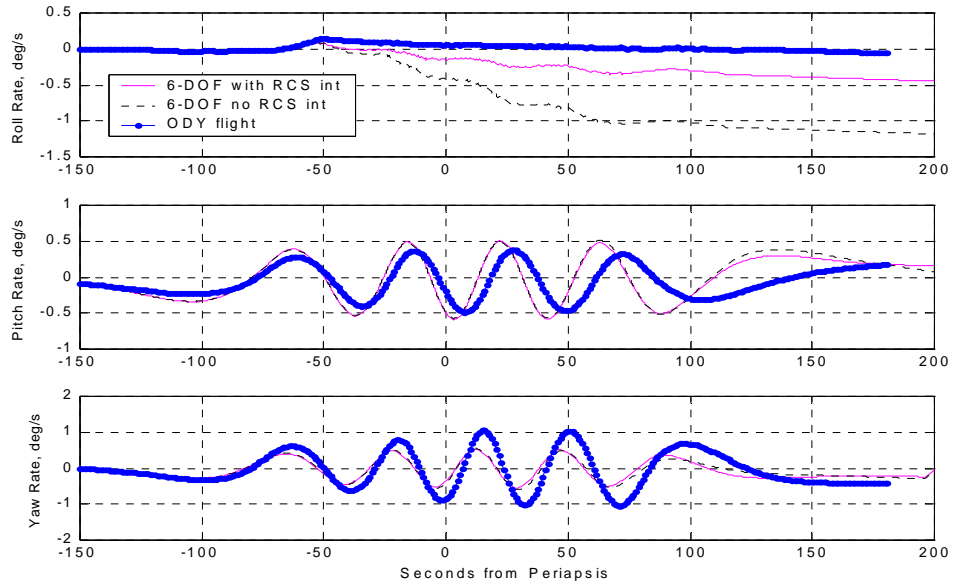


**Figure 8.4.** Attitude Rates Comparison of POST 6-DOF Simulation to Flight Data, Orbit 24, RCS Model Active, Thrust Model Active

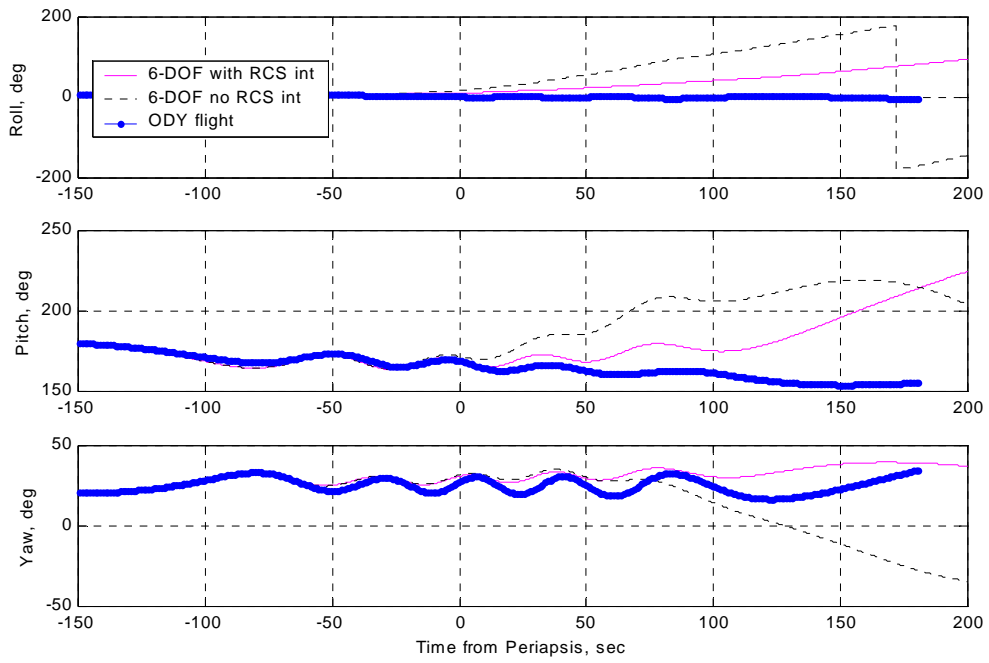


**Figure 8.5.** Aero Angles Comparison of POST 6-DOF Simulation to Flight Data, Orbit 24, RCS Model Active, Thrust Model Active

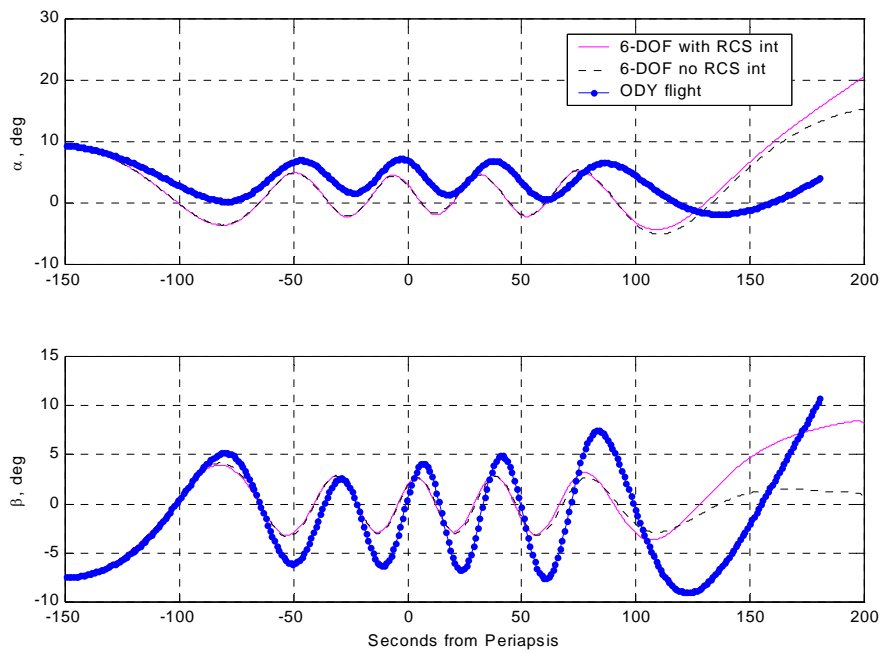


**Figure 8.6.** Attitude Comparison of POST 6-DOF Simulation to Flight Data, Orbit 24, RCS Model Active, Thrust Model Active

The fact that a noticeable difference between the flight data and the predictions still exist can be partially attributed to uncertainties in the modeling parameters, such as the center of mass location, moments of inertia, and modeling the thrust impulse as a square wave. There are also uncertainties in the density predictions, which are input into the RCS effects subroutine. The RCS effects subroutine contains errors introduced in the plume model, the DSMC simulations, and the interpolation scheme used.

In an effort to reduce the overall error and match the 6-DOF simulations more closely to the flight data, moment coefficient multipliers were added to the POST simulations. There are three multipliers used to multiply the delta moment coefficients returned from the RCS plume effects subroutine by a user specified value. Variation of each of the multipliers individually showed that the roll rate was the most sensitive, which was expected since the roll rate showed the most change with the inclusion of the RCS plume effects. The rolling moment coefficient was then multiplied by a constant for each orbit (starting with orbit 46) to match the simulation results for roll rate with the actual flight data. The roll moment multipliers versus the maximum density reached by the spacecraft for each orbit are shown for orbits 46 – 100 in [Figure 8.7](#). A few trends can be observed. First, all of the multipliers are greater than unity. This implies that the model is consistently under predicting the effects on the rolling moment. Also, the multipliers decrease with increasing maximum atmospheric density for an orbit. The multipliers range from about 1.3 to 2.6. [Figure 8.8](#) shows the multipliers for orbits 250 – 300. The same trends mentioned previously are observed for these orbits. One major difference between the early and later passes is the values of the multipliers. For these latter orbits the multipliers are much larger, ranging

from 2.5 to 7.5. As aerobraking proceeded, the values of the multipliers at the same maximum density appear to have increased.

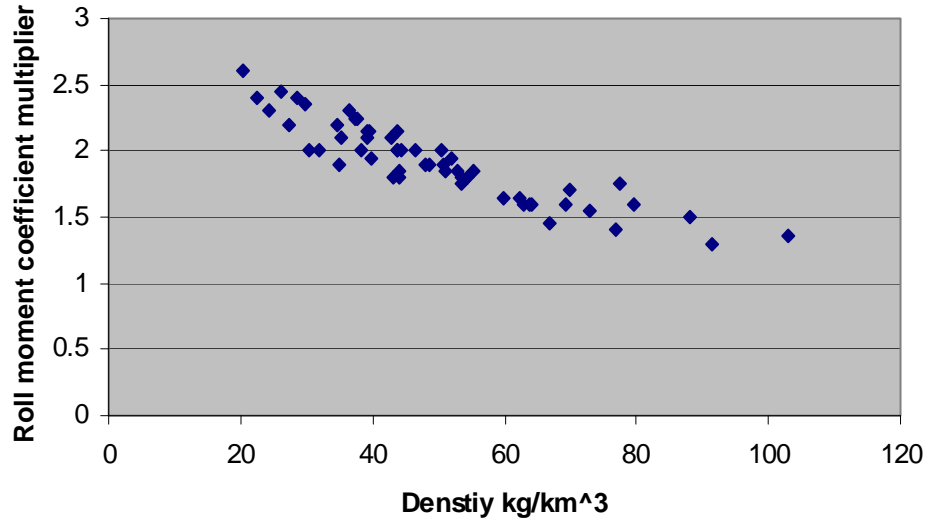


**Figure 8.7.** Variation of RCS Rolling Moment Coefficient Multipliers with Maximum Density for Orbits 46 – 100

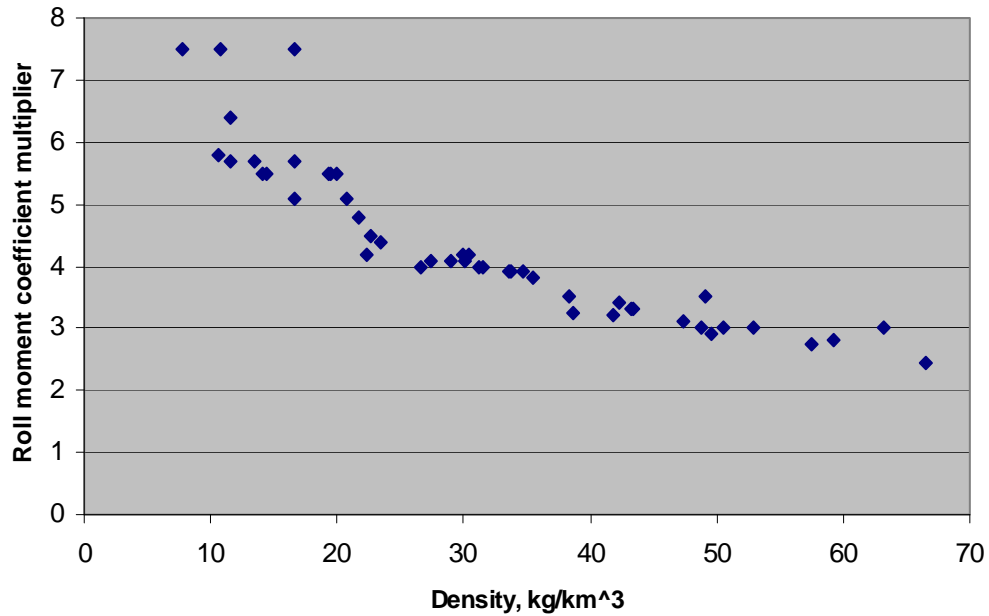


**Figure 8.8.** Variation of RCS Rolling Moment Coefficient Multipliers with Maximum Density for Orbits 250 – 300

## Chapter 9. Conclusions

This study details the modeling of RCS plume effects and the inclusion of these effects into 6-DOF simulations of the Mars Odyssey during aerobraking. The modeling was performed by calculating the effects of RCS firings on the aerodynamics of Odyssey using a DSMC computer program which simulated the low-density, atmospheric flow about the spacecraft and the flow introduced by the RCS jet plume. The aerodynamic effects were extracted and incorporated into a database that was used in the 6-DOF simulations.

A methodology for describing the RCS plume was developed which used a Navier-Stokes code, VNAP, to simulate the internal nozzle flow which then provided nozzle exit conditions for a source flow model of the plume. A parametric study of various computational variables and a comparison of results based on another Navier-Stokes code, GASP, for an MGS RCS nozzle showed that the VNAP results provided a sufficiently accurate representation of the internal nozzle flow.

A source flow model developed by Woronowicz was modified and used to make the plume flowfield predictions. The Woronowicz model had been previously modified to include parameters that controlled the aspect ratio (ratio of the width to the length) of the plume and a density multiplier that assisted in calibrating the model to other flowfield data. A comparison of source flow model predictions to GASP predictions for the plume flowfield of an MGS nozzle suggested that the aspect ratio factor should be lowered from the value of 1.6 used for Odyssey to a value of 1, and the density multiplier raised from a value of 0.4 to 0.7. These changes would result in a slimmer and more elongated plume flowfield. The computational mesh on which the

source flow model was applied was also modified to reduce the computational time necessary to run the model.

The model was modified to automatically extract an iso-density surface from the flowfield that could then be used as an inflow boundary for the DSMC simulations. The iso-density surface is shown to be a reasonable approximation to an iso-momentum ratio surface for rapidly expanding plumes and is used in place of a Bird breakdown condition for defining the region between continuum and transitional flow. Flowfield parameters (density, velocity, and temperature) were extracted from the source flow solution and provided inflow boundary conditions expressed as an out gassing surface condition for the DSMC simulations. The sensitivity of the shape and size of the iso-density surface to various model parameters as well as to nozzle exit conditions predicted by various methods was examined. All of the methods examined gave plume shapes and centerline properties that appear to be reasonable but the results could not be assessed further in the absence of experimental data.

A complete database describing the changes in aerodynamic coefficients caused by various RCS thruster firings over a range of attitudes and atmospheric densities was created. DSMC simulations were performed to determine the RCS effects at a select few attitudes and densities, and an interpolation scheme was developed to fully populate the database for use in the 6-DOF program. The interpolation scheme used greatly reduced the number of DSMC simulations necessary and provided relatively accurate results.

The RCS plume effects were incorporated into a subroutine that could be called during POST 6-DOF simulations. 6-DOF simulations were performed with and without the RCS effects and the results were compared to flight data. These comparisons showed that the inclusion of the

RCS effects provided significant improvement in the agreement between simulations and flight data especially in the roll rate. However, the comparisons indicate that the RCS effects are being under predicted which suggests that the plume might be larger and denser than predicted. Adjustments to the aspect ratio parameter and density multiplier in the source flow model could be used to account for these larger effects, but the availability of accurate plume flowfield data or flight measurements that are a more direct measure of plume impingement would be a highly desirable aid to further plume model calibrations.

Overall, the methodology used to determine the RCS plume flowfield and to determine the RCS interactions with the aerodynamics of Odyssey were satisfactory. The comparisons of 6-DOF simulations with flight data indicate that the methodology produced the correct qualitative trends and suggest that further refinements of the methodology would be useful for future aerobraking missions.

## **Chapter 10. Future Work**

During this study, a comparison of the source flow model versus a detailed CFD solution for the MGS plume flowfield suggested that the aspect ratio factor in the source flow model should be reduced and the density multiplier should be increased from the values that were used to calculate the Odyssey plume flowfield. This would result in a plume with less influence on the aerodynamics. Whereas 6-DOF comparisons with Odyssey flight data suggest that the aerodynamic impact of the plumes are being underestimated. Increasing the aspect ratio factor or the density multiplier would result in a larger plume with greater effects on the aerodynamics. Further study is needed to calibrate the model for a variety of test cases to determine proper values for the aspect ratio factor and the density multiplier.

Further study is also recommended to test the accuracy of using simple isentropic flow models to generate nozzle exit conditions.

## References

1. Bird, G.A., *Molecular Gas Dynamics and the Direct Simulation of Gas Flows*, Clarendon Press, Oxford, 1994.
2. Thompson, T.W., Plaut, J.J., Weitz, C.M., "Mars Exploration Program 2001 Mars Odyssey Orbiter," NASA Research Announcement, Proposal Information Package, July 2001.
3. Rault, D.F., "RCS Plume Effect of Spacecraft Aerodynamics During Aerobraking Maneuver," 20<sup>th</sup> International Symposium on Rarefied Gas Dynamics, Institute of Mechanics, CAS, Beijing, China, August 1996.
4. Woronowicz, M.S., and Rault, D.F.G., "On Plume Flowfield Analysis And Simulation Techniques," *AIAA Paper No. 94-2048*, AIAA/ASME 6<sup>th</sup> Joint Thermophysics and Heat Transfer Conference, Colorado Springs, Colorado, June 1994.
5. Cline, M.C., "VNAP: A Computer Program for Computation of Two-Dimensional, Time-Dependent Compressible, Viscous, Internal Flow," Los Alamos Scientific Laboratory, *LA-7326*, Los Alamos, New Mexico, Nov. 1978.
6. "Model for Prediction Orbiter PRCS Plume Impingement Loads and Heating," *JSC-26507*, NASA Johnson Space Center, June 1995.
7. Glass, C.E., "Numerical Study of Rarefied Hypersonic Flow Interacting With a Continuum Jet," NASA Langley Research Center, *NASA/TP-2000-210551*, Hampton, Virginia, November 2000.
8. Shane, R.W., and Tolson, R.H., "Aerothermodynamics of the Mars Global Surveyor Spacecraft," M.S. Thesis, George Washington University, March 1998.
9. LeBeau, G.J., and Lumpkin III, F.E., "Application Highlights of the DSMC Analysis Code (DAC) Software for Simulating Rarefied Flows," *Computer Methods in Applied Mechanics and Engineering*, Vol. 191, Issue 6-7, 2001, pp. 595-609.
10. Powell, R.W., Striepe, S.A., Desai, P.N., Braun, R.D., Brauer, G.L., Cornick, D.E., Olson, D.W., Petersen, F.M., Stevenson, R., "Program to Optimize Simulated Trajectories, Version 5.2 Utilization Manual," October 1997.